Alma Mater Studiorum - Università di Bologna

Department of Physics and Astronomy
Laurea Magistrale in Astrophysics and Cosmology

Star Clusters as Gamma Ray emitters

Presentor:
Archana Purushothaman

Supervisor:
Prof. Marcella Brusa
Co-Supervisors:
Dr. Giada Peron
Dr. Stefano Gabici

Academic year 2021-2023

Contents

List of Figures

List of Tables

List of Symbols

Symbol	Description
γ	Gamma
ϵ	epsilon
π^0,$\pi^{\pm}$	pion
p	momentum
$\mu^{\pm}$	Muon
ν_e,ν_μ	neutrino
α	Spectral index
e	electron
z	redshift
F	Flux
L	Luminosity
η	Acceleration efficiency
v	velocity
n	Density of medium
P	pressure
Γ	Adiabatic constant
σ	standard deviation

List of Acronym

Acronym	Full form
CR	Cosmic Ray(s)
eV	Electron volt
EeV	Eta electron volt
GeV	Giga electron volt
MeV	Mega electron volt
Myr	Million year(s)
TeV	Tera electron volt
PeV	Peta electron volt
ISM	Interstellar Medium
SNR	Supernova remnant
WR	Wolf Rayet
WTS	Wind Termination Shock
VHE	Very High Energy
GLAT	Galactic Longitude
GLAT	Galactic latitude
LAT	Large Area Telescope
FoV	Field of View
TS	Test statistic
$\mathcal{L}$	Log like value
FGL	Fermi Gamma-ray LAT
WISE	Wide-Field Infrared Survey Explorer
IR	Infrared

Abstract

Cosmic rays have been an enigma since their discovery nearly a century ago. The bulk of the particles that constitute cosmic rays have Galactic origins, but the a complete understanding of the origin and acceleration of these particles are still not clear. From the direct and indirect observations of Galactic cosmic rays, a probable source for the acceleration of these particles seems to be Supernova remnants (SNR). But this hypothesis cannot satisfactorily explain the high energy cosmic rays and the prominent features in their spectrum observed near Earth. Another probable source for cosmic ray acceleration are star clusters, where the birth and evolution of massive stars accelerate the cosmic rays through stellar winds and later as supernovae.

The limitations imposed by the diffusive nature of cosmic rays on direct observations forces us to study the gamma-rays, resulting from the interaction of cosmic ray particles and the eventual decay of resulting neutral pions, as an indirect tracer of cosmic rays. Thus, by examining the star clusters for possible gamma-ray counterparts, we can test the possibility of them being cosmic ray accelerators.

This work focus on the study of a large number of star clusters to identify the possibility of them being the source for cosmic ray acceleration. By utilizing the multi-wavelength observations and correlating catalogs, this thesis work establishes that star clusters indeed emit in γ-ray regime and the energy provided by the mechanical luminosity is enough to accelerate cosmic rays. It also gives a comprehensive morphological model of the γ-ray sources associated to star clusters with constraints on the luminosity and acceleration efficiency of the cosmic rays.

Chapter 1

Cosmic Rays

1.1 Introduction

Cosmic rays (CR), despite their name coined by Robert Millikan, are made up of matter rather than photons. This is because these 'rays' appear to get deflected by the magnetic fields. They consist of charged particles of about 90% protons, 9% alpha particles and the remaining 1% are nuclei of heavier elements.

Victor Hess, an Austrian physicist, wanted to study the penetrating radiation that seemed responsible for the discharge of electroscopes in the early 20th century. In 1912, Hess took flight in a hot air balloon with electrometers to study the radiation intensity and went on to make the discovery that earned him the Nobel prize in 1936 - Cosmic Rays. Domenico Pacini, an Italian scientist also studied this 'radiation' intensity by using a submarine. These studies led to the understanding that this rate of discharge of the electroscope changes with height and depth from the Earth's surface (discharging almost 4 times faster than the ground level at 16000 feet above Earth's surface) and therefore to the understanding that the 'radiation' responsible for this is of extraterrestrial origin (Blasi (2013), T.K. & Stanev (2006)).Kolhörster and Gockel's balloon flight confirmed Hess's findings. Clay and later Compton's survey also found that this 'radiation' is dependent on latitude (discharging faster at the poles than the equator implying the CR propagation should be diffusive). Millikan's experiments carried out between 1923 and 1926 cemented the fact that this radiation was extraterrestrial.These CRs contribute $\sim 1\ eV/cm^3$ to the local energy density of the Galaxy. This is similar to the contributions from other components of the ISM to the energy densities (Amato 2018). The galactic and extra galactic CRs are differentiated by their energies and confinement conditions (Gabici 2019). The length of the path of the particle deflected in the magnetic field can be calculated by the Larmor radius as (Eq. 1.1),

$$R_{larmor} = p/qB \quad \text{(pc)} \tag{1.1}$$

These are calculated by assuming that a charge q is deflected by the magnetic field B and the charge has a momentum p.

If this Larmor radius is less than the halo size h, the charge is contained inside the halo. Most of the CR energy density is carried by the high energy particles ($\gtrsim$ GeV energies) and a typical value of B is 0.1-10 μG. The Larmor radius of protons at $10^{15}eV$ is of the order of ≈ 1 pc (Hoerandel (2004)) for 1μG magnetic field. This

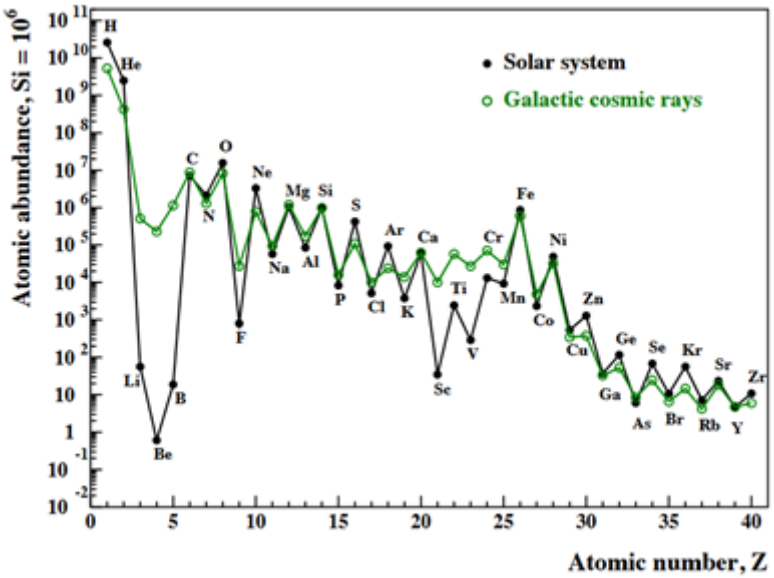

Figure 1.1: Composition of galactic CR compared to solar composition *(Credit: Tatischeff & Gabici (2018))*

is several orders smaller than the typical size of the halo, h around a few kpc ($\sim$ 0.3 kpc -3.4 kpc) Using the confinement condition, the energy for galactic CR can be calculated by Eq. 1.2-1.3.

$$\frac{E(eV)}{B(G)}(kpc) = R_{Larmor} < h \tag{1.2}$$

$$E < 10^{18}\frac{h}{kpc}\frac{B}{\mu G}(eV) \approx 10^{17}eV - 10^{20}eV \tag{1.3}$$

CR with energies less than 10^{15} eV are considered of galactic origin due to these confinement conditions. CR with energies above 10^{19} eV are of extra-galactic origin since their Larmor radius in the magnetic field is the same order of size as the halo and therefore these particles cannot be confined or accelerated further (Gabici et al. (2019)).

In order to maintain the CR energy density, the power injected to the ISM by the CR sources should be $P_{CR} \sim W_{CR}/\tau_{res}$ where τ_{res} is the residence time of CR in the Galaxy and W_{CR} is the total energy of the CR estimated to be around 10^{55} ergs. The residence time is calculated by the comparison of chemical composition of CR to solar composition.

An overabundance in lighter nuclei elements like Li, Be, B can be seen in the cosmic ray composition with respect to the solar composition (Figure 1.1). This can be explained by spallation, where the lighter nuclei are produced by the collision of heavier nuclei in CR primary particle with the protons and helium nuclei in the interstellar medium during their journey. The secondary species or the ones created through spallation will have a steeper spectrum when compared to those accelerated at the sources, called primary species. Information about the transport of cosmic rays can be derived from the ratio of abundance of secondary particles to primary particles. Consider that the heavy primary species, indicated by p (eg. Carbon) ,

converts into secondary species s (eg. Boron) through spallation. Assume that n represents the number density of the respective species, n_{ISM} is the density of the ISM, σ_s is the relevant spallation cross section,τ_{res} is the residence time and c is the speed of light (Gabici et al. (2019)).

$$\frac{n_s}{n_p} = n_{ISM}\tau_{res}\sigma_s c \tag{1.4}$$

The spallation cross-sections are calculated from observations from Earth. This can also be calculated by using Eq.1.4 with the CR secondary-to-primary ratios (for example the B/C ratio), typical density of the ISM ($\approx$ 1 $particle/cm^3$), and the residence time in the Galactic disk (of the order of few Myr).

From this the CR power can be calculated as $P_{CR} \sim 10^{41}$ erg/s.

1.2 CR spectrum

The all-particle spectrum, also known as the local CR spectrum (CR measured locally outside the Earth's atmosphere), consists of differential energy spectra of different particles of CR as a function of kinetic energy per nucleon of the particles. The flux of particles reaching the Earth per unit time, per surface, per solid angle per unit energy interval, called differential flux or differential energy spectra. The energy ranges from approximately 1 GeV ($10^9 eV$) to several EeV ($10^{18} eV$) (Longair 2013). At energies below 1 GeV/nucleon, the magnetized wind from the Sun diffuses the CR in the ISM, inhibiting the low energy particles from reaching Earth and modulates the spectrum into a bend at low energies.

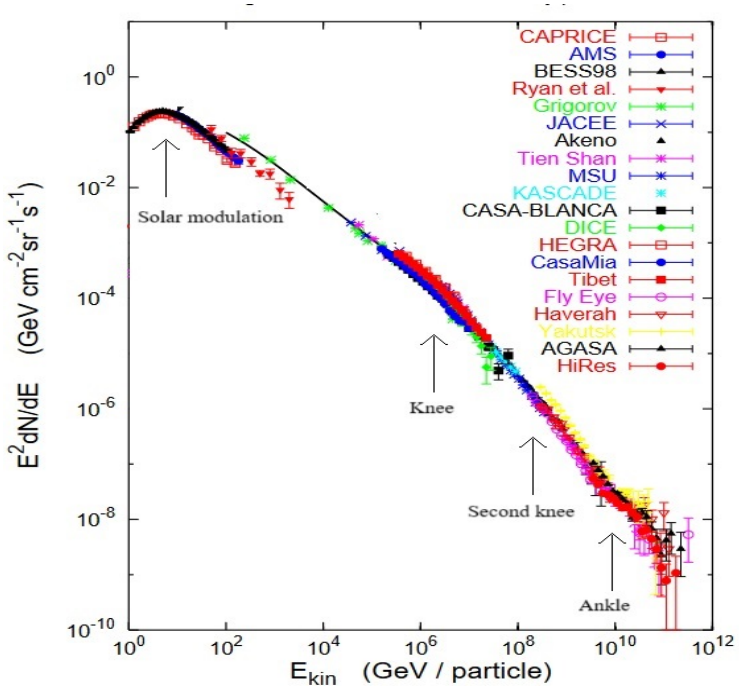

Figure 1.2: Cosmic ray spectrum as a result of various collaborations *(Credit:Hillas (2006))*

After solar modulation effects are taken into account, the differential energy spectra roughly follows a universal power law spectral model. The differential energy

spectra can be represented as $N(E) \propto E^{-x}$, where x is the slope of the spectrum (Figure 1.2). The slope of the differential flux is ~ 2.7. There are many distinguishing features of the CR spectrum. After 3×10^{15} eV (3 PeV), the slope steepens to ~ 3.1, known as the 'knee' of the spectrum. This continues until 10^{19} eV (1 EeV), where the spectrum steepens to ~ 3.3, known as the 'ankle' of the spectrum, which is the contribution from extra galactic cosmic rays. After the ankle, the slope of the spectrum returns to ~ 3.1. There is also the 'second knee' at about 5×10^{17} eV which is less pronounced. The propagation effects and the transition from galactic to extra-galactic components explains these observed features. The CR between energies between the knee and ankle is thought to be the transition from galactic to extra-galactic components. The CR acceleration mechanism is rigidity dependent, and the protons only reach a maximum energy of 5 PeV. For Nuclei heavier than Helium, the energies reach Z (atomic number of nuclei) times the maximum energy. This means that the knee can be interpreted as a superposition of cutoff of different nuclei.

1.3 Transport of CR

The estimation of crossing time by assuming the height of the galactic disk H and speed of light c for a relativistic CR ($t_{cross} = H/c$) is approximated to a few kyr, which is 3 orders of magnitude less than the real value of residence time estimated in section 1.1 by the abundance ratio of chemical composition of CR. This means that the transport of CRs are diffusive. The irregularities in the galactic magnetic field deflecting the CRs are able to explain this phenomenon. By assuming a purely diffusive regime, mean free path λ and diffusion length l_d, the diffusion coefficient D can be calculated as Eq. 1.5 - 1.6.

$$D \approx \lambda c \tag{1.5}$$

$$l_d \approx \sqrt{Dt} \tag{1.6}$$

By assuming typical values of thickness of disk as 300 pc and time of 3 Myr from the measurement of the grammage, the average diffusion coefficient is found to be around $3 \times 10^{28} cm^2/s$ ($\sim 1 GeV/nucleon$).

CR diffusion is energy dependent. By spallation measurements at different energies, the time for spallation in disk, t $\propto E^{-0.3}$. From Eq. 1.6, the diffusion coefficient D is proportional to E^{-s} with s ranging from 0.3 to 0.6. The energy injection spectrum in the Galaxy Q_{CR} can be calculated (Eq.1.7).

$$Q_{CR} = \frac{N_{CR}}{t_{disk}} \propto N_{CR}(E) D(E) \propto E^{-s} \tag{1.7}$$

Here the s ranges from 2.1 to 2.4.

1.4 Origins of CR

Even though they have been observed for more than a century, the sources of CR remain elusive. Due to their diffusive properties, the CRs have nearly isotropic arrival direction when approaching Earth. This makes it difficult to retrace them to their origins.

The following conditions must be satisfied to explain the origins of Galactic CRs (Gabici 2023):

- Sources must inject CR with a power of 10^{41} erg/s to ISM
- CR should be accelerated to energies above the knee
- The differences observed in chemical composition must be explained
- The energy spectrum of CRs injected to the ISM should be close to a power law proportional to E^{-s} with s$\approx 2.1 - 2.4$.

Two of the main acceleration sites proposed included Supernova Remnant(SNR) and Star Clusters (SC) for galactic CRs.

1.4.1 Supernova and supernova remnants

Up until a few years ago, the primary candidate for CR production and acceleration sites were isolated Supernovae and Supernova Remnants (SNR). This was first proposed by Baade and Zwicky in 1936, supported by the idea that the power released by a supernova explosion, a total of 10^{51} ergs, was high enough to explain the CR acceleration. This hypothesis was known as SNR paradigm. The rate of total kinetic energy of the ejecta injected to the ISM comes to around 10^{42} erg/s which equals 10% efficiency rate. If 10% of this mechanical power is converted to accelerating particles, observed CR power can be attained. This assumes an explosion rate of 3 supernova per 100 years.

Based on the presence of Hydrogen Balmer lines in the optical spectrum at 656.3 nm (Longair 2011), Supernova can be broadly divided into Type I (No Hydrogen lines present) and Type II (Hydrogen lines present). Type I can be subdivided into type Ia (Silicon lines present at 615 nm), type Ib (No Silicon lines present, Helium lines present at 481.7 nm), type Ic (No Silicon lines and weak/no Helium lines present at 481.7 nm). Type Ia, generally referred to as thermonuclear supernova, occurs in a binary system with a white dwarf accreting matter from companion star until it reaches the Chandrasekhar limit ($M \approx 1.44 M_{solar}$). It then explodes in a thermonuclear explosion with no remnant. Type Ib,Ic and II is referred to as core collapse supernova, occurs in stars with high masses(M$> 8 M_{solar}$). The star continues nucleosynthesis till the core is iron(Fe) and lighter materials are being processed in the outer layers giving it an onion like structure. The fusion is no longer active in the core, and neutrino losses become significant and contraction due to gravity occurs. The infalling material bounces back when the gravity is balanced by the neutron degerancy and causes a shockwave and explodes as supernova. The shock expands and forms a supernova remnant (SNR).

Acceleration mechanism

The magnetic fields deflects the particles in the SNR several times through the shock wave. The particles get accelerated due to this repeated deflections and attain a maximum energy before escaping the SNR shock acceleration site. The low energy CRs attain energy each time they pass they get deflected by magnetic fields which is explained by the Fermi acceleration mechanisms (Fermi (1954)). The Fermi I acceleration mechanism describes the acceleration of CR by shocks and the Fermi II acceleration describes the CR acceleration due to local disturbances in velocity by turbulent magnetic fields. The diffusive shock acceleration theory (DSA) explains the Fermi acceleration of strong shocks created while interacting with moving magnetised perturbations. This is a specialization of the Fermi I for strong shocks. This was proposed by Bell (Bell (1978)), Blandford & Ostriker (Blandford & Ostriker (1978)) and other authors. According to this theory, CR are deflected and accelerated by the magnetic field discontinuity between the shock and surrounding medium. The CR passes through this discontinuity multiple times, before it escapes the system. The larger gyro radius of CR results in a higher increase in velocity, meaning they get accelerated to relativistic speeds through Fermi acceleration. Typically, the particles are injected with a maxwellian distribution and contribute to a powerlaw spectrum. The minimum momentum p_{min} for a particle to transition from maxwellian distribution $p_{thermal}$ to a powerlaw can be determined by a factor q_{inj} which ranges from 3-4 (Eq.1.8).

$$p_{min} = q_{inj} * p_{thermal} \tag{1.8}$$

Where, $p_{thermal} = \sqrt{2m_p K_B T}$ given mass of proton m_p, temperature of the medium T and Boltzmann constant K_B.

$$\frac{dN}{dE} \propto E^{p+2} \tag{1.9}$$

The DSA theory for strong shocks leads to a differential spectrum with a powerlaw $\propto E^{-2}$ (Eq.1.9).

Due to uncertainty in shock dynamics and energy losses in transportation, the spectral index can range between 2.3 - 2.5, which explains the observed CR spectrum.

Limitations

SNR paradigm has several limitations, both theoretically and observationally (Gabici et al. (2019), Amato (2014)).

- **Hillas criterion**: The accelerated CR attain a maximum energy after which it is no longer bound to the accelerator and escapes the accelerator. The maximum energy can be calculated by the Hillas criterion. The Larmor radius (R_{Larmor}) is assumed to be typical size of the accelerator (r_{sh})(approximated as the maximum radius of the shock) for a shock moving with a velocity (u_{sh})

in a magnetic field B. The maximum energy (ϵ_{max}) that can be attained by a charged particle can be calculated (Eq. 1.10).

$$\epsilon_{max} \approx \left(\frac{r_{sh}}{pc}\right)\left(\frac{B}{\mu G}\right)\left(\frac{u_{sh}}{1000km/s}\right) TeV \tag{1.10}$$

This means that to attain PeV energies, B $\geq 100\mu G$ is needed for a SNR expanding to a radius of few parsecs with a velocity of 1000 km/s.

- **Spectrum**: from the ratio of B/C (Boron to Carbon) from the CR composition, the CR transport is expected to be affected by a factor $\propto E^{-0.3}$ to $E^{-0.6}$. For attaining spectrum above the knee, the SNR sources must inject a spectrum steeper ($\propto E^{-2.1}$ to $E^{-2.4}$) that the calculated spectra for test particle ($\propto E^{-2}$).

- **Isotropic abundance**: Chemical abundance in CRs namely $^{58}Fe/^{56}Fe$ ratio, and the overabundance of $^{22}Ne/^{20}Ne$. The abundance of $^{22}Ne/^{20}Ne$ is $\sim$ 5 times more than that of the solar wind. This is not explained by SNR hypothesis alone.

- **PeV energy spectra**:The young SNR observed seems to have a cutoff below $\sim$10 TeV, making them ineligible as Pevatron candidates (sources emitting in the PeV energies). Middle aged SNRs like W44 and IC443 both seemed to have cutoff at relatively low energies as well. The maximum attainable energy is in the order of $\sim$100 TeV in the most optimistic scenarios. This is limited by the age of the remnant as well as the size of the remnant. This is way less than that seen in the high energy tail which extends up to PeV energies.

1.4.2 Star Clusters and Superbubbles

A possible alternative site for CR acceleration could be Star clusters and Super bubbles was suggested by Montmerle (Montmerle (1979)). Star formation usually occurs in dense, clustered environments (Bykov et al. (2017)). These star clusters contain astrophysical objects of various ages, metallicity, mass, size and evolutionary stages. Most massive stars are born in clustered environments where they spent their whole lifetime and finally explode as supernova.

Massive stars, with mass M $> 8M_{solar}$ are expected to end their lives in a supernova explosion. These are mostly O and B type stars. These are luminous blue stars with similar evolution, which are sometimes seen in associations,could be the sites of CR acceleration. These OB stars produce stellar winds, which ejects matter from the surface of a star in a continuous supersonic outflow with a speed of $\sim$ 1000 km/s. These winds enrich the surrounding ISM with mechanical energy, momentum and recycled nuclear material produced in the star. The energy released, when added across their typical lifetimes of $\sim 10^7$ years amount to almost the same energy as released by a supernova explosion for massive stars. These stellar winds also interact with the stellar winds of other members of the cluster in their vicinity. Combining this with the subsequent supernova explosions in the clusters, low dense hot ($\geq 10^6$ K) cavities called super bubbles are formed. Super bubbles provide a

confinement mechanism that is efficient enough to produce and accelerate CR up to high energies.

The massive stars eject outer layers after their Hydrogen burning phase (Gupta et al. (2020)Morlino et al. (2021)). These layers are ejected at supersonic speed by the stellar wind to a few pcs. This creates a wind termination shock (WTS) in the ISM. The star continues its evolution and continues to eject the outer layers. Stars with initial mass above $\sim 20 M_{solar}$, go through a Wolf- Rayet (WR) phase. This WR phase is one of the key aspects that define the star clusters as CR accelerators. The stellar winds associated with these massive stars, with typical velocity of ~ 1000 km/s can produce power up to 10^{38}erg/s in the cluster. This power can produce effective particle acceleration to multi TeV energies. After this phase, the star cannot sustain thermonuclear fusion and begins to explode as core collapse supernovae. The star explodes with a massive energy injection into the ISM as well as a shock. The CRs are assumed to be accelerated at the wind termination shock (WTS) or by the SNR shock. These are driven by Fermi 1 and Fermi 2 mechanisms as well as shock acceleration mechanisms (see section 1.4.1). Also in superbubbles, containing supernova remnants as well as ejecta from stellar winds from massive OB stars are very large. Due to their size and turbulent exterior, they confine and drive particle acceleration well up to PeV energies of the CR spectra. This exceeds the power that can be attained by an isolated supernova by at least 2 orders of magnitude.

The assumption of star clusters and super bubbles as CR accelerators could explain a few discrepancies that were unexplained by the supernova paradigm. The work done by Bykov et al 2015 considers the particle acceleration in Superbubbles by assuming an ensemble of stochastic shocks in the turbulent medium. Another model assumed acceleration of the CR at collective wind termination shocks. Recent model explained that the magnetic field is amplified at the wind termination shock, which pushes the CR acceleration to well above the knee. This is also considered more efficient than acceleration around a single supernova. More studies by Higdon and others (Klepach et al. (2000),Hoerandel (2004),Prantzos (2012)) support the star cluster and superbubble origins of CR.

As mentioned above, the $^{22}Ne/^{20}Ne$ abundance can be explained by the presence of the ejecta from the Wolf- Rayet stars swept into the ISM through the stellar winds (Higdon & Lingenfelter (2005),Gupta et al. (2020)). WR stars have an onion like structure which is made up of products of nucleosynthesis in the stars core. This includes fusion products up to iron in the core and lighter elements fanning outwards. This is a solution to the CR neon isotropic problem. The carbon stage of Wolf Rayet stars converts all ^{14}N into ^{22}Ne before explosion through a set of chain reactions. Even if the assumption that 5 percent of this ^{22}Ne is acquired by the CR can explain the $^{22}Ne/^{20}Ne$ abundance. This ^{22}Ne can be acquired by the CR over several scenarios (Higdon et al 2005, Gupta et al 2020).

Star clusters also explain the presence of other refractory elements that are found in abundance in CRs. For example, the ^{60}Fe is mainly produced by the capture of neutrons by Fe isotopes in massive stars and core collapse supernova. ^{60}Fe has a short half lifetime of $\sim$ 2.6 Myr. The Cosmic Ray Isotope Spectrometer (CRIS) instrument found that the mean time between nucleosynthesis and acceleration of ^{60}Fe is consistent with star clusters. For a supernova scenario, this time means that ^{60}Fe cannot be accelerated by the same supernova. The time required for transport

of CR should not exceed the half-life period of ^{60}Fe and the distance should be less than the diffusion length of this time (< 1 kpc). For the observed abundance in the CR, it is likely to be originated from a nearby cluster like the Scorpius-Centaurus association.

The enhanced super-bubble core metallicity could explain why the majority of cosmic rays can be accelerated in the superbubble even with a smaller number of supernovae explosions and achieve the typical efficiency of conversion of CRs to γ-ray (Higdon & Lingenfelter (2005)). Furthermore, the diffuse galactic γ -ray emission studies show that OB stars have similar radial distribution as CRs with a 1/r radial distribution. This can also distinguish the Hadronic and Leptonic origin of CRs by using the star cluster model at TeV energies .

1.5 Gamma rays and Cosmic rays

Cosmic rays interact with the ambient interstellar medium (ISM) and photons, which produces gamma rays (Longair 2011). These gamma rays can be originated from two different scenarios: Hadronic and Leptonic.

Hadronic scenario

When CR particles collide inelastically with the ISM, γ-rays are produced. Pions are produced as a result of proton-proton interaction, which later decay into γ-rays. There are 3 possible outcomes of this proton-proton interaction (Eq. 1.11).

$$p_{ISM} + p_{CR} = \begin{cases} \pi^0 + p + p \\ \pi^+ + \pi^- + p + p \\ \pi^+ + n + p \end{cases} \tag{1.11}$$

The charged pions decay to produce muons(μ), muon neutrinos(ν_μ) and muon anti neutrinos ($\bar{\nu_\mu}$). These decay into electrons and positrons with a mean decay time of 10^{-8} s. The π^0 decays into two γ-ray photons with a mean decay time of 10^{-16} s.

$$\pi^0 \rightarrow 2\gamma$$

It is estimated that 10 percent of the energy of protons is obtained by the photon. The energy loss rate of the proton is dependent on the cross section of collision (σ_{pp}), the inelasticity $f \sim 0.5$, and the density of the ambient medium (n) and initial energy of the proton (E_p) (Eq. 1.12).

$$\frac{dE_p}{dt} = n\sigma_{pp} f c E_p \tag{1.12}$$

The radiative cooling time of protons can be calculated as Eq. 1.13,

$$\tau_{pp} = \frac{1}{n\sigma_{pp} f c} \approx 6 \times 10^7 \left(\frac{n}{cm^{-3}}\right)^{-1} yr \tag{1.13}$$

Leptonic scenario

γ-ray photons can also be produced by processes like Inverse Compton scattering, Bremmstrahlung emission or Synchrotron radiation. The basic of these processes are given below.

- Inverse Compton scattering:

  The Inverse Compton scattering is due to the interactions of electrons with photons. High energy electrons e_{HE} scatter low energy γ-ray photons(γ_{LE}) and produce high energy γ-ray photons (γ_{HE}) in the MeV energy and above.

  $$e_{HE} + \gamma_{LE} \rightarrow e'_{LE} + \gamma_{HE}$$

  At higher energies, the inverse compton effect is suppressed due to higher energies of electron with respect to the rest mass energy. An energy cutoff can be observed in the photon spectrum at energies $\sim$ 50 TeV. The cooling time of the electron (τ_{IC}) can be calculated from the radiation energy density (U_{rad}) and the electron energy E_e (Eq.1.14). U_{rad} is the energy density of the cosmic microwave background radiation (CMB) $\sim 0.26 eV/cm^3$.

  $$\tau_{IC} \approx 3 \times 10^8 \left(\frac{U_{rad}}{eV cm^{-3}}\right)^{-1} \left(\frac{E_e}{GeV}\right)^{-1} yr \tag{1.14}$$

- Bremmstrahlung emission :

  Electrons undergo scattering with the stationary nucleus (N) in the ISM and deflects the nucleus. Non-thermal Bremmstrahlung emission is produced when the electron undergo Coulomb interaction with an atomic nucleus, causing the electron to decelerate after being deflected. The difference between energies of the CR electron before e^- and after collision e'^- is emitted as γ-ray photons.

  $$e^- + N \rightarrow e'^- + \gamma$$

  The cooling time (τ_{brems}) is dependent on the number density of the ambient medium (n) (Eq. 1.15).

  $$\tau_{brems} \approx 4 \times 10^7 \left(\frac{n}{cm^{-3}}\right)^{-1} yr \tag{1.15}$$

- Synchotron radiation:

  When electron transverses through a magnetic field (B), a Lorentz force is produced which deflects the electron and causes it to spiral around the magnetic field lines. This accelerates the electron and produces synchotron radiation.

  $$e^- + B \rightarrow e'^- + \gamma$$

  The cooling rate (τ_{syn}) is dependent on the magnetic field (B) and energy of the primary electron (E_e). The magnetic field is dependent on the number density (n) of the ambient medium (Eq. 1.16).

$$\tau_{syn} \approx 1.2 \times 10^7 \left(\frac{B}{\mu G}\right)^{-2} \left(\frac{E_e}{TeV}\right)^{-1} yr \tag{1.16}$$

1.5.1 Observations

The acceleration of CR particles can be studied by indirect methods that trace their presence from their interaction with the ambient medium. The γ-ray emission (refer Section 1.5) can be used to observe possible CR accelerators. In recent years, several star clusters have been observed to emit high energy diffuse γ-ray emission and have shown evidences of CR acceleration. These detections have been done by ground based telescopes like High Altitude Water Cherenkov Telescope (HAWC), High Energy Stereoscopic System (HESS), Very Energetic Radiation Imaging Telescope Array System (VERITAS), MILAGRO and space based γ-ray telescopes like Fermi-Large Area Telescope (Fermi LAT) and Energetic Gamma Ray Experiment Telescope (EGRET). Major candidates of these emissions are from star clusters regions like Cygnus OB2, Westerlund 1, Westerlund 2, NGC 3603 and 30 Dor C in the Large Magellanic cloud. Some of them are discussed below.

Cygnus OB2

The Cygnus OB2 has been of particular interest. Cygnus OB2 has an age of 3.5 million years and has a spectrum of energy extending up to 150 TeV with a peak at 10-100 GeV (Ackermann et al. (2011)). The γ-ray luminosity of this source above 10 GeV is around 3×10^{34} erg/s (Aharonian et al 2018). The total energy injected by the star cluster is calculated to be 2×10^{52} ergs that could account for the CR acceleration easily.

The TeV counterpart MGRO J2031+41 in the Cygnus region (Figure 1.3a) has been studied by the MILAGRO telescope (Abdo et al. (2007)). This source coincide with the Cygnus OB2 region. Cygnus OB2 also coincide with TeV J2032+413 observed by MILAGRO with observed diffuse γ-ray emission upto 10 TeV energy.

Westerlund 1

Westerlund 1 is the most massive star forming region in our Galaxy containing over 150 OB stars and 24 Wolf-Rayet stars. HESS J1646–458 (Figure 1.3b) is associated to this cluster with a γ-ray luminosity of $\sim 2 \times 10^{35}$erg/s between 0.1 to 100 TeV energies (HESS Collaboration et al. (2011), Aharonian et al. (2022)). Westerlund can account for the required injection energy needed for particle acceleration of cosmic rays.

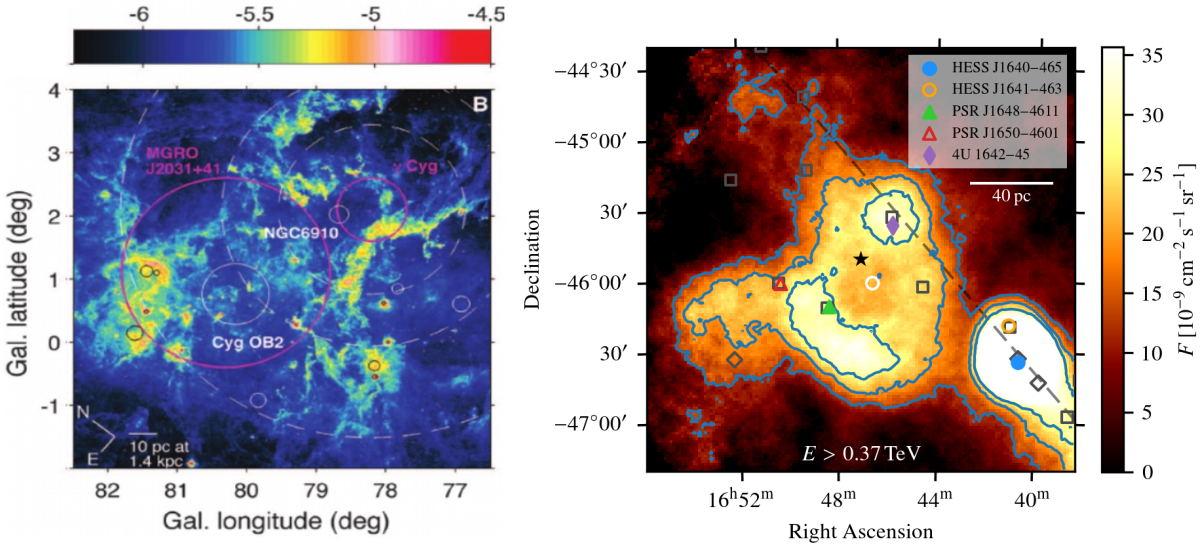

Figure 1.3: Left: Observation of γ-ray emission from Cygnus region. The γ-ray emission is observed by MILAGRO telescope from a source that is embedded inside the Cygnus OB2 region. The white circle represents the Cygnus OB2 region with the magenta circle represents MGRO J2031+41 *(Credit:Abdo et al 2007)* Right :Observation of γ-ray emission from source HESS J1646-458 that seems to be associated with Westerlund 1 region. The position of Westerlund 1 is marked by the black star symbol; *(Credit :Aharonian et al .2022).*

Other SC associated with γ-ray emission

Other star cluster sources of γ-ray emission are explained briefly.

Westerlund 2 is a massive stellar cluster with age around 2-3 Myr. This sources has been detected at very high γ-ray energies by HESS. The source shows a hard spectrum extending upto 250 GeV (zhi Yang et al. (2018)). This source has γ-ray luminosity of $\sim 10^{35}$erg/s above 1GeV.

Westerlund 40 is one of the largest star forming clusters near the galactic plane with age less than 1 Myr. This source seems to be associated with three γ-ray sources detected by Fermi-LAT (Sun et al. (2020)). The CR luminosity of this region was detected to be around 6×10^{32}erg/s above 1 GeV.

Young massive stellar cluster NGC 3603 has been observed to produce γ-rays in the 1 GeV to 250 GeV range. NGC 3603 is regarded as one of the massive HII regions in our Galaxy, aged around 2 Myr. The study of this region revealed a hard γ-ray spectrum extending upto 250 GeV (zhi Yang & Aharonian (2017)).

Observations of LMC by Fermi-LAT revealed high energy $\gamma-$ray emission coming from massive star forming region 30 Doradus C (Abdo et al 2010). 30 Doradus C is surrounded by 6 subclusters. $1-10$ TeV $\gamma-$ray luminosity of $\sim 10^{35} erg/s$ has been observed by the HESS collaboration (HESS collaboration 2015) from this region. Due to the absence of other possible point like sources, revealed that this emission is most likely to be powered by cosmic ray interactions.

Goals of thesis

As shown in the Introduction, SNR has been extensively studied as galactic CR accelerators and yet they fall short to account for some properties shown by CR. Star clusters have been proposed as an alternative source of astrophysical object capable of CR acceleration and capable of producing Pevatrons.

The thesis pursues to achieve the following objectives:

The first part of the thesis aim to analyse the available star cluster catalogs and correlate them to γ-ray source catalog by checking if their positions have possible overlaps with each other. To ascertain the significance of these matches, 1000 synthetic catalog is also simulated via Monte Carlo technique, and matched with the star cluster catalog. The significance of the correlation is calculated to ascertain the correlation of the matching.

The second part of the thesis consist of characterizing the energetic and morphological properties of selected Fermi sources that shows a correlation to star cluster from the first part. By selecting a few Fermi sources and studying their energetics using the SED analysis and their luminosity, the efficiency of these sources to accelerate the CR can be studied. By doing this, the study is intended to give a comprehensive model to observe cosmic rays in future studies.

The thesis is organized as follows:

- Chapter #1 describes the Basics of CR, CR sources, γ-ray and observations of CR, providing a scientific background and context for the thesis.
- Chapter #2 gives a brief description of the telescopes (Gaia, WISE and Fermi) used to construct the catalogs for the study. This section also provides the description of the data in the relevant star cluster and gamma ray catalogs.
- Chapter #3 describes the methodology used to correlate the catalog for possible associations. The first section is divided into matching and simulation. The matching section explains the methods for correlating catalogs, and the simulation part describes the method and principles used for simulation of synthetic catalogs. The latter section presents the result of the correlation.
- Chapter #4 describes the principles and methodology of Fermi analysis of selected sources. The energetic and luminosity results of the analysis are explained at the end of this chapter.
- Chapter #5 describes the summary and conclusion of the study

Chapter 2

Telescopes and Ancillary data

2.1 Gaia Telescope

2.1.1 Telescope

Gaia is a space observatory of European space Agency (ESA) whose goal is to chart a three-dimensional map of the Milky Way galaxy in order to reveal the composition, formation and evolution of the galaxy (Gaia collaboration 2023). Gaia targets objects brighter than magnitude 20 in a broad photometric band that range between near-UV (330 nm) and near infrared (1050 nm). Gaia entered its operational orbit around the Sun-Earth L2 Lagrange point. It started taking data on July 25th, 2014. The mission aims to construct by far the largest and most precise 3D space catalog ever made, totaling approximately 1 billion astronomical objects, mainly stars, but also planets, comets, asteroids and quasars etc. The Gaia satellite is composed of 2 identical telescopes separated by an angle of 106.5 °. Each telescope has a primary mirror with a collecting area of 0.7 m^2. The focal plane consists of 106 CCDs aligned such that the images by both telescope project on it. The satellite has 3 components (Figure 2.1):

- The Astrometric instrument takes up most of the focal plane and collects source images in the Gaia white-light pass band G (covering the range 330-1050 nm.
- The Photometric instrument is realized through two prisms dispersing the light entering the field of view of two dedicated sets of CCDs. The Blue Photometer (BP) operates over the wave-length range 330–680 nm, while the Red Photometer (RP) covers the wavelength range 640–1050 nm.
- The Spectroscopic instrument, also called the radial-velocity spectrometer (RVS) collects medium resolution spectra over the wavelength range 845–872 nm, centered on the Calcium triplet region.

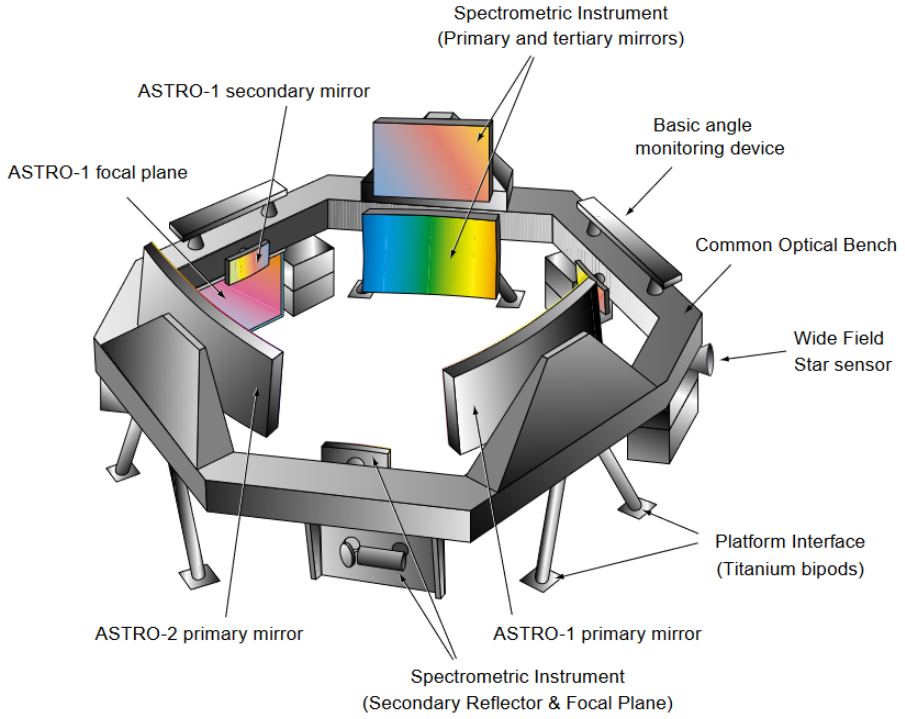

Figure 2.1: instrument setup of Gaia showing 2 astrometric instruments, ASTRO-1 and ASTRO-2 separated by 106.5 °, as well as the spectroscopic instrument which contains the photometric instrument and the radial velocity spectrometer, mounted on a Titanium platform*Credit: Zeeuw 2002*

2.1.2 Catalog description

Gaia Data Release 3 (Gaia DR3) has been released on 13 June 2022 containing information of stars collected between 25 July 2014 and 28 May 2017 spanning a period of 34 months of data collection. The full data release contains a total of 1,467,744,818 sources. The data for the star clusters is taken from the catalog of clusters referred to in the paper by Hunt and Reffert (Hunt & Reffert (2023)). In the Paper (Hunt & Reffert (2023)), data taken from the Gaia data release (Gaia DR3) catalog is studied and exposed to a search for open clusters with magnitude < 20, producing a single homogeneous star cluster catalog in the paper. This star cluster catalog contains 6818 open clusters, 228 moving clusters and 121 globular clusters adding up to a total of 7167 clusters.

The Star clusters in the Gaia catalog has a total of 7167 sources. Gaia catalog contains information about the ages of stars given by the column *'log_age_50'*. This is the 50^{th} percentile of logarithm of cluster age ranging from ~ 3 Myr (log_age_50$\sim$6.5 to $\sim$ 10 Gyr (log_age_50$\sim$10). The age of the cluster can be an indicator to the process inside the stellar cluster. The lifetime of a star is connected to the initial mass of the star (Vieu et al. (2022)) (Eq. 2.1),

$$log_{10}\ t\ [yr] = 9.598\ -\ 2.879\ log_{10}\ M + 0.6679\ (log_{10}\ M)^2 \qquad (2.1)$$

From this, the most massive stars (mass $>$ 8 M_{solar}) start to explode around $\approx$ 35 Myr. The lifetime of a star with $\sim 150 M_{solar}$ (the maximum mass limit for

a star at equilibrium) has a limit at 3 Myr. Star clusters in their early ages, ie, age < 3 Myr, have little to no supernova explosions meaning that the particles are considered to be accelerated by only by stellar wind. At ages between 3 Myr to 35 Myr, Star clusters begin to have a considerable amount of supernova explosions. At this stage, both supernovae and stellar winds inject energy to the ISM which aids in the acceleration of CR. At the largest ages, i.e, ages > 35 Myr, the massive stars have exploded into supernovae and there are no more massive stars to produce stellar winds anymore. Therefore, the contribution to CR acceleration decreases considerably.

For this study, the clusters in the catalog are divided in accordance with their age into 3 groups as follows (Figure 2.2):

- **Group 1**: clusters with age less than 3 Myr (*'log_age_50'* < 6.5)
- **Group 2**: clusters with age between than 3 Myr and 35 Myr ($6.5 \leq$ *'log_age_50'* ≤ 7.55)
- **Group 3**: clusters with age greater than 35 Myr (*'log_age_50'* > 7.55)

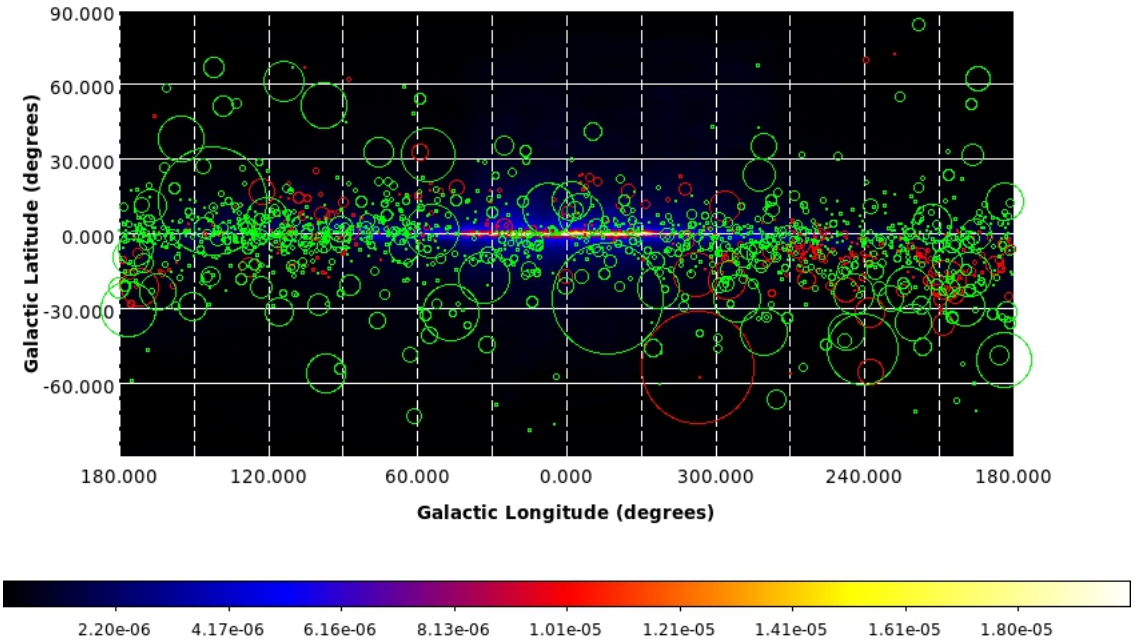

Figure 2.2: Different groups of Gaia SC source data positions plotted over the galactic interstellar diffuse emission model is *gll_iem _v07*: Group 1 represented by cyan circles, Group 2 represented by red circles, Group 3 represented by green circles.

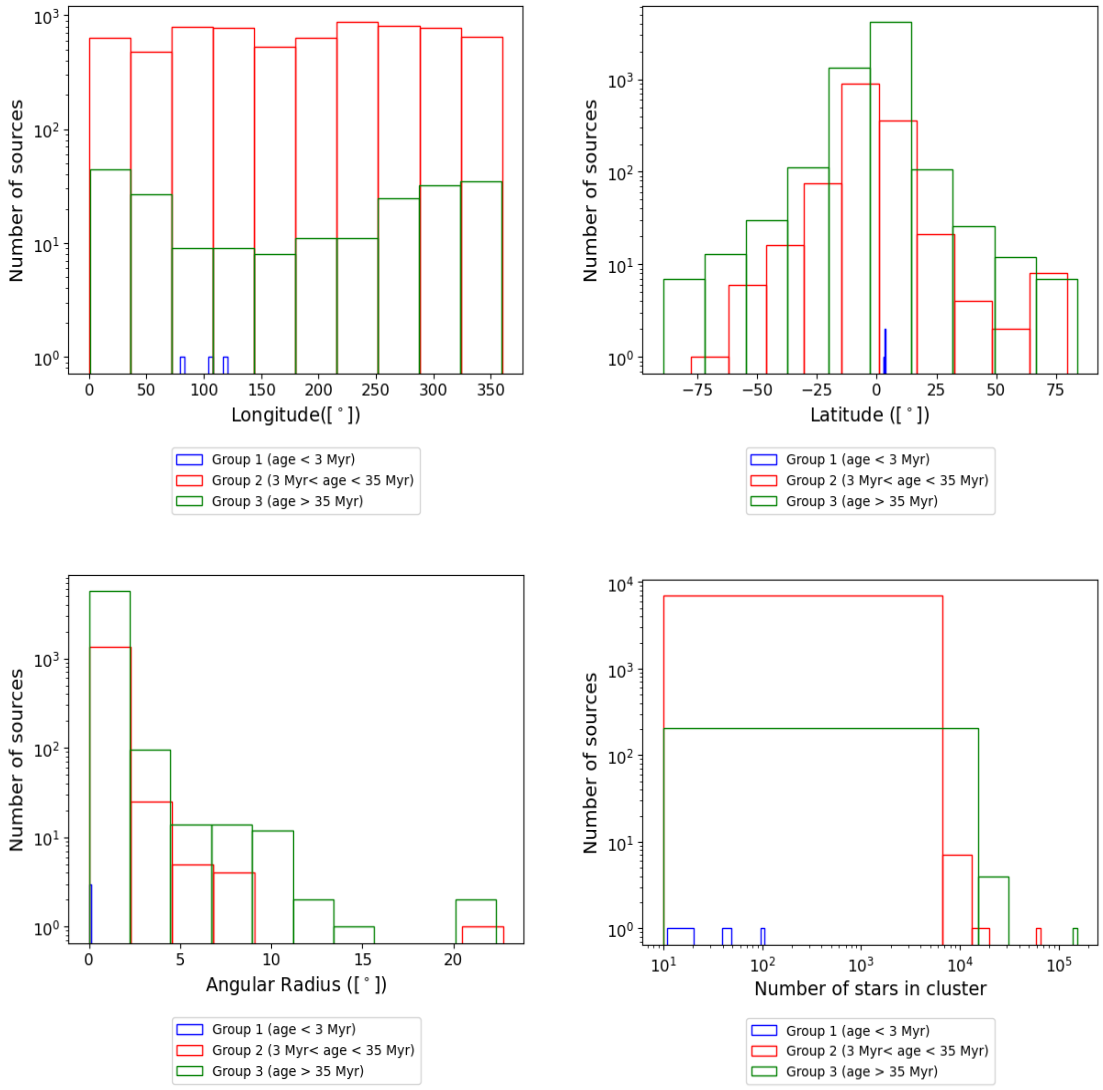

Figure 2.3: Histogram representing distributions of different age groups in Gaia SC catalog. Blue represents the Group 1, green represents Group 2, Red represents the Group 3. Top left: Distribution of Longitude, Top right: Distribution of Latitude, Bottom left: Distribution of the angular radius of 50 percent of the cluster members, Bottom right: Distribution of number of stars inside the angular radius of 50 percent of the cluster members

The distribution of various parameters of different age groups is seen in Figure 2.3. The longitude is indicated in the catalog by *'l'* (ranging from 0 ° to +360 °) and latitude for the from the column *'b'* (ranging from -90 ° to +90 °). The radius of the star cluster used for the study is taken from the radius that contains 50 % of the cluster members, given by the *'ang_radius_50'* column in the catalog. The number of stars in this radius is indicated by *'n_stars'* which ranges from 10 to 153797 stars inside the cluster. The distribution of different parameters of each age group can be seen in Figure 2.3. A higher number of sources in group 3 is distributed close to the galactic plane with small number of outliers beyond $|b| < 60°$, whereas group 2 seems to be evenly distributed. Group 3 has smaller angular radius ($< 5°$) while Group 2 has a variety of angular radius upto ~ 20 °.

2.2 WISE telescope

2.2.1 Telescope

The Wide-Field Infrared Survey Explorer (WISE) satellite (Figure 2.4) was launched by NASA on December 14, 2009. It was decommissioned and was reactivated as NEOWISE in Sept. 2013. It was placed at a height of 525 km in a sun synchronous orbit from Earth. It has a field of view of 47 arc minutes. WISE takes pictures of the sky every 11 seconds, orbiting the Earth 15 times a day. It circles around poles along the terminator, a line where day turns into night. This ensures that the solar panels are always aligned to recharge. The WISE telescope has a 40 cm diameter aperture and four infrared detectors. It surveys the sky in Infrared wavelength bands of 3.4, 4.6, 12 and 22 microns. It has angular resolutions of 6.1", 6.4", 6.5", and 12", respectively. It is enclosed in a cryostat with frozen hydrogen called cryogen. This is to ensure that the telescope remains in 12 Kelvin, the 12-micron and 22-micron detectors operate at less than 8 Kelvin and the 3.4- micron and 4.6-micron detectors operate at 32 Kelvin. The main objectives are:

- To find nearest and coolest stars.
- To find and study the asteroids in our galaxy.
- To study the most luminous galaxies.
- To study obscured stars.

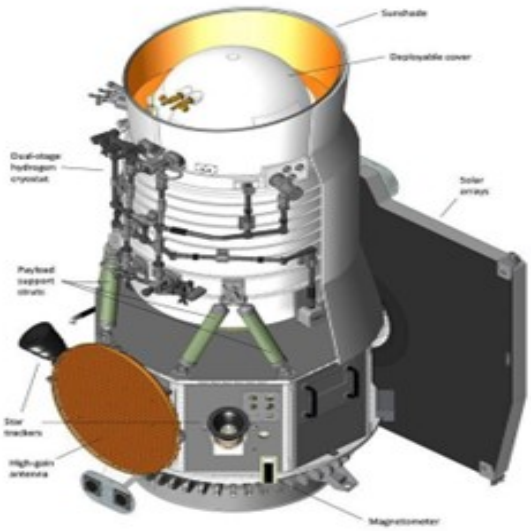

Figure 2.4: Instrument setup of WISE
Credit: https : //www.jpl.nasa.gov/news/press$_k$its/wise − launch.pdf

2.2.2 Catalog description

The star clusters with age less than ∼1 Myr due to their younger age are mostly not observed in the visible range of the electromagnetic spectrum because they are

obscured by the hydrogen cloud cocoon and dust, in which they form. These young massive stars (mainly OB stars) produce ultra-violet photons which create zones of ionized gas, called HII regions, and dust surrounding them. The IR emission is observed due to the re-emission from hot interstellar dust. Galactic HII regions are observed mostly in the Radio and Infrared wavelengths. HII regions give information of the present star formation due to their short lifetime. HII regions are tracers of massive stars, that are expected to accelerate CRs. These HII regions are surveyed by WISE in the 12-micron and 22-micron bands. HII regions have a characteristic mid-infrared (MIR) morphology, where the $\sim 20\mu m$ emission (coinciding with the ionized gas traced by the radio continuum emission) is surrounded by the the $\sim 10\mu m$) emission. WISE can detect these regions with its $22\mu m$ band with a resolution of 12 arcseconds with a sensitivity of 0.6 mJy.

The WISE data is taken from the paper "WISE catalog of galactic HII regions" by Anderson et al.2014. The galactic HII regions is identified by WISE $12\mu m$ and $22\mu m$ images.

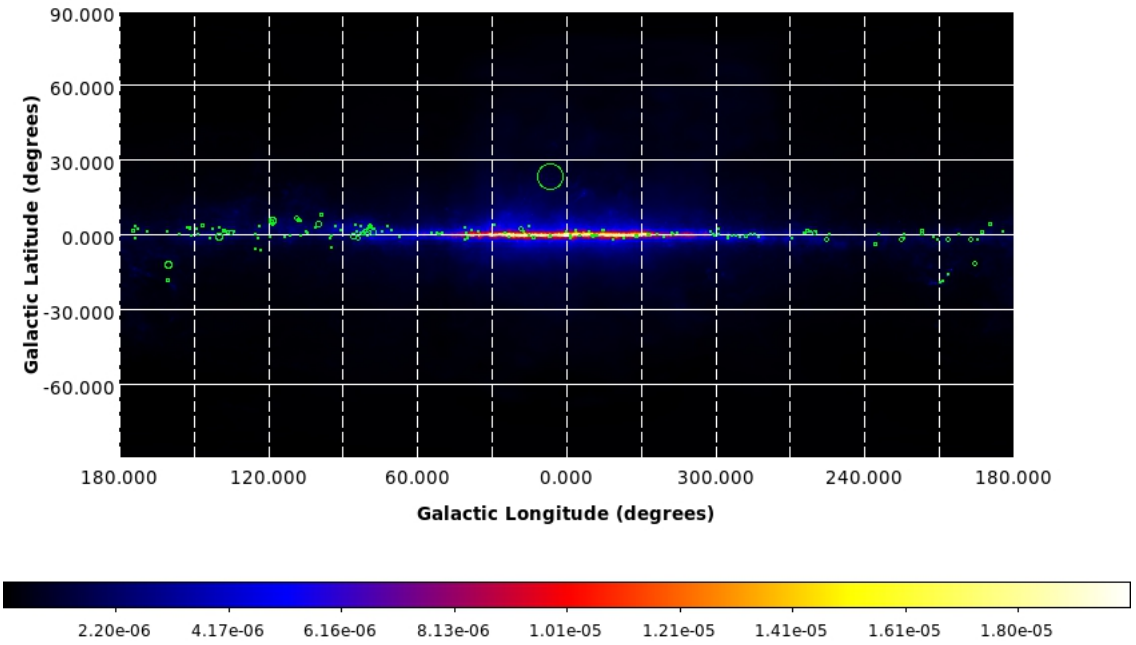

Figure 2.5: Positions of WISE HII regions plotted as green circles over the galactic interstellar diffuse emission model is *gll_iem _v07*

The current dataset is the V2.2 version. It contains 8412 sources (Figure 2.5). This includes known HII regions and candidate HII regions. The candidate HII regions that are spatially coincident with radio continuum emission, but do not yet have any Radio recombination line or $H\alpha$ observations. In addition, some well known candidates are also added. The latitude of WISE sources range from $-20°$ to $+20°$, and longitude from 0 to $+360°$ (Figure 2.6). The angular radius of sources range from 5 arcseconds (0.0014°) to 18666 arcseconds (5.185°). 1785 sources have their distances measured through various methods.

The longitude and latitude are given by the *'GLong (deg.)'* and *'Glat(deg.)'* columns. The radius is given in arcseconds by *'Rad(arcsec.)'* column and converted to ° for this work. The flux is given in column *'WISE 22um (Jy)'* and projected distance is taken from 'Dist *(kpc.)'* column.

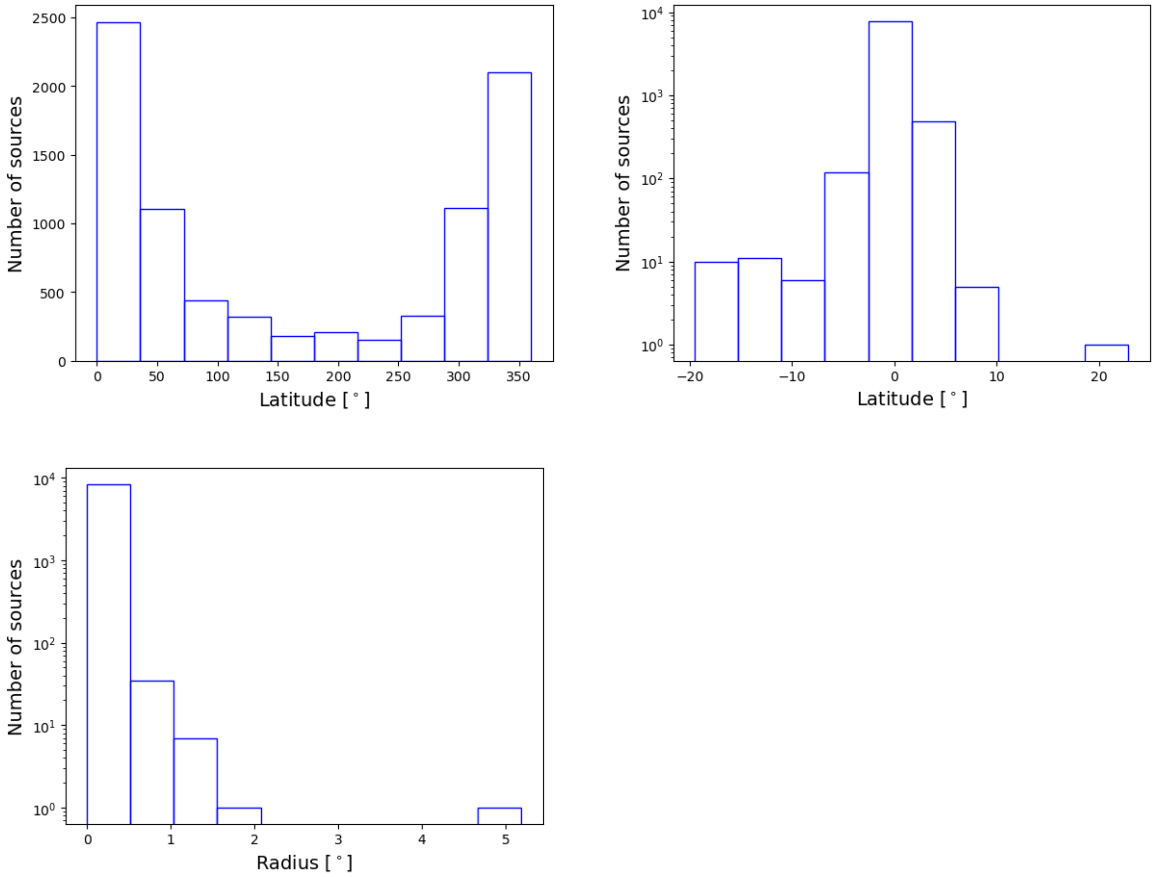

Figure 2.6: Distribution of latitude, longitude and radius of sources in the WISE catalog

2.3 Fermi Gamma-ray Space Telescope

2.3.1 Telescope

The Fermi Gamma-ray Space Telescope, originally called the Gamma-Ray Large Area Space Telescope (GLAST) by NASA has been surveying the high-energy γ-ray sky since June 11, 2008 . It is in a low Earth orbit (LEO) at an altitude of 550km, and surveys the γ-ray sky in the energy range 20 MeV upto $\sim$ 1 TeV energies. Fermi carries two instruments: the Large Area Telescope (LAT) and the Gamma-ray Burst Monitor (GBM).

Gamma-ray Burst Monitor (GBM)

The GBM consists of 12 sodium iodide detectors for capturing X rays and low-energy γ-rays, and 2 detectors made of Bismuth Germanate for high-energy γ-ray. The photomultiplier tube detects a Gamma Ray Burst (GRB), producing a higher flash than when the X-ray/low energy γ-ray strikes the sodium-Iodide detectors, allowing to find the direction of the GRB by combining 3-4 detector signals. The Bismuth Germanate detectors placed on opposite sides of the spacecraft are high-density material that provides better sensitivity at high energies, namely at 150 keV to about 30 MeV, while the sodium Iodide detector is working in the low energy range namely 8 keV - 1 MeV.

Large Area Telescope (LAT)

Fermi LAT scans the sky in the range from 30MeV up to $\sim$ TeV energies. The Fermi LAT has a field of view (FoV) which includes 20% of the sky which covers the whole sky in 3 hours. The FoV is approximately $\sim$ 2.7 steradians above 1 GeV. The Point Spread Function (PSF) is $\sim$5 $^\circ$ at 100 MeV and $\sim$0.8 $^\circ$ at 1 GeV improving to $\sim$ 0.1 $^\circ$ above 20 GeV. The PSF decreases with energy as $E^{-0.8}$.

The four main subsystems in the Fermi LAT are:

- Tracker
- Calorimeter
- Anti-coincidence Detector
- Data Acquisition System

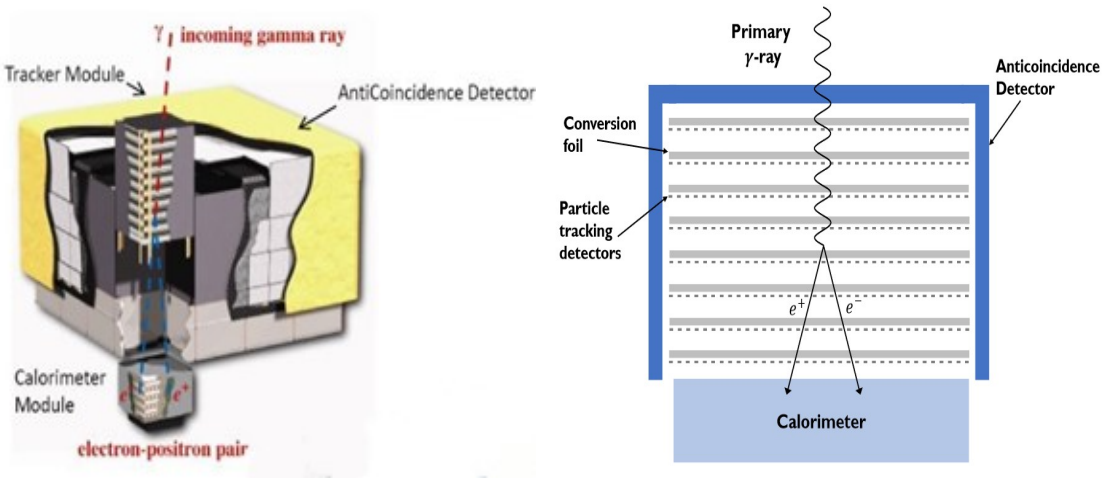

Figure 2.7: Left: Instrumentation setup of Fermi LAT telescope, Right: Simplified view of Tracking module

The electron and positron are produced when high energy γ-ray undergoes pair conversion process with the foil made of high metallicity material (Figure 2.7a). Here, the material used is Tungsten aligned in 16 layers which facilitate conversion of γ-rays to $e^- - e^+$ pairs. These tungsten strips are placed between 36 Silicon strip detectors which act as trackers for the $e^- - e^+$ pairs (Figure 2.7b). Beneath the tracker is a calorimeter composed of an 8-layer array of 12 CsI (Ti) crystals each to determine the γ-ray energy and development pattern. A segmented anti-coincidence Detector covers the tracker array to reject charged-particle background events, along with a programmable trigger and data acquisition system (DAQ).

2.3.2 Catalog description

The catalog utilized in this thesis is the fourth Fermi LAT catalog of γ-ray sources (4FGL where FGL stands for Fermi Gamma-ray LAT). The third data release (DR3) contains 12 years of observations data in the 50 MeV - 1 TeV energy range taken from August 4, 2008, to August 2, 2020 (collaboration et al. (2022)). The current version of LAT data is P8R3 which stands for pass 8 data. These sources include pulsars, SNR, blazars, binaries etc., counting to a total of 6658 sources. There are 79 columns in the catalog including galactic latitude and longitude, associations, spectrum type, class of sources. The 2157 unassociated sources have no clear counterpart in other wavelengths.

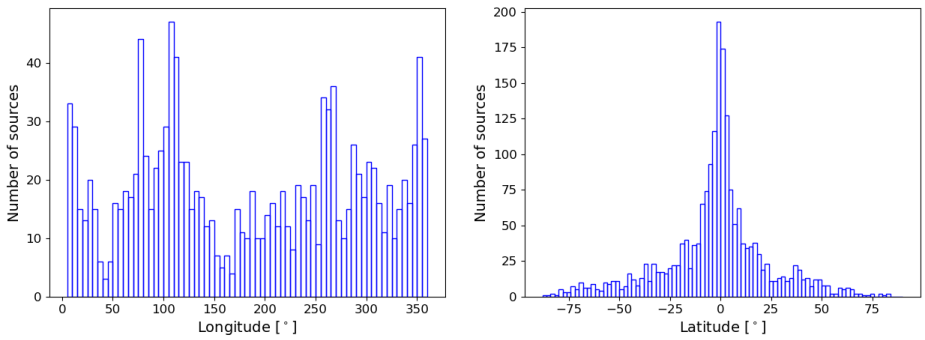

Figure 2.8: Distribution of Galactic latitude and longitude of sources in the Gamma catalog

The 4FGL-DR3 catalog column *'CLASS 1'* represents high-confidence association and *'CLASS 2'* represents low-confidence association of sources. This gives the possible associations of the γ-ray sources. For this thesis, the 2157 γ-ray sources selected are unidentified or unassociated. This is done by removing all known associations of sources from the 4FGL-DR3 catalog. However, some of these sources seem to have values in the low confidence column, meaning that there is a chance that the sources can be associated into some other source categories. The unknown sources of γ-rays are indicated by the 'unk' or blank in the *'CLASS 1'* and empty indications in the *'CLASS 2'*. The empty columns in *'CLASS 2'* ensures that the sources selected for the study doesn't have any possible counterparts/associations. This assures that the remaining sources in the catalog used are unidentified and includes 1982 sources for this study. The longitude and latitude are given by the 'GLON' and 'GLAT' columns. This distribution of the latitude and longitude is given in Figure 2.8 .

Chapter 3

Matching and Simulation

The goal of this work is to discern if star clusters are γ-ray emitting sources. This section correlates the star clusters to γ-ray sources by comparing the distance between them. The unidentified γ-ray sources observed by Fermi (refer to section 2.3.2) may be associated to the star clusters observed in other wavelengths.

An algorithm (refer section 3.1) was written that calculates the angular distance between the star cluster catalog (Hereafter SC catalog) sources and γ-ray (Hereafter Gamma catalog) sources and then compares this separation to the angular radius of the star clusters. 1000 synthetic catalogs are generated with Monte Carlo simulation (described in section 3.2) and matched to the SC catalog using the matching algorithm. The matches obtained with the real and synthetic catalog is compared to quantify the significance of the correlation seen using the real catalogs.

3.1 Matching

The γ-ray sources given in the Gamma catalog are checked to see if their positions overlap with any of the star clusters in the given SC catalog. The angular distance is calculated between each Gamma catalog source and SC catalog source (Eq. 3.1 - 3.3). Then the condition is applied that the angular distance between these sources should be less than that of the angular radius of the star cluster. This ensures that the Gamma catalog source is overlapping with the SC catalog source, and has a higher probability of associated to the SC catalog source. If the condition is met, the sources are said to be 'matching'.

To discern if the matches from the above algorithm are random or not, the sources in the SC catalog is matched with synthetic catalogs. Synthetic catalogs are simulated using the Monte Carlo extraction explained in the following section.

3.2 Simulations

Monte Carlo simulation is used generate synthetic catalogs by randomly extracting the distribution of galactic latitude and longitude of the sources in the Gamma catalog as explained below. 1982 values of longitude and latitude are extracted randomly from the cumulative distribution to create a synthetic catalog with same length of the Gamma catalog. 1000 synthetic catalogs having 1982 sources each with

random positions are simulated using this method. Each of the sources in these 1000 synthetic catalogs undergo the matching algorithm with the SC catalog sources.

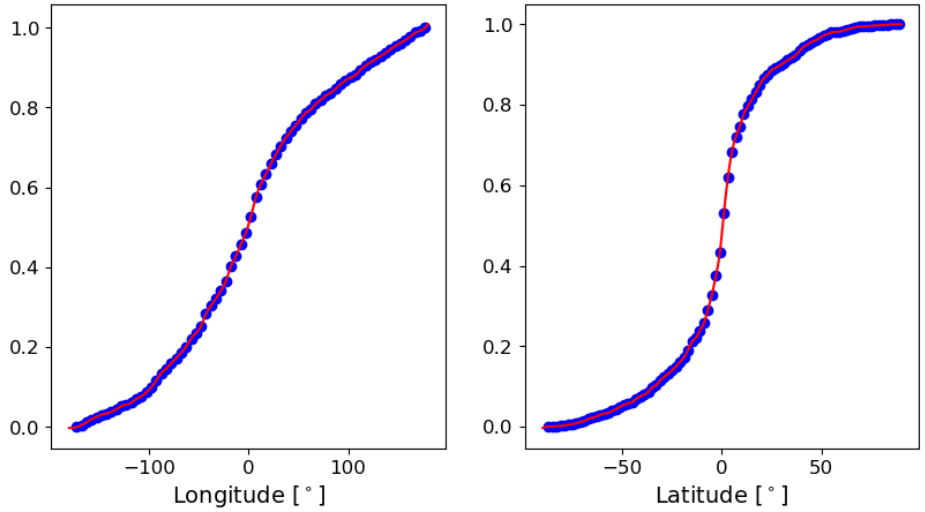

Figure 3.1: Cumulative distribution from Gamma catalog (blue points) and its interpolation(red curve) used for the Monte Carlo simulation to create synthetic catalogs. The bin size of 0.1 degree is taken for both distributions

The distribution of galactic longitude and galactic latitude is studied (Figure 2.8). Each of these distribution is sampled into bins (bin size of 5 degrees for the longitude and 1 degrees for the latitude) and then integrated to get the cumulative distribution. This is normalized to 1 and interpolated to obtain a finer grid . 1982 values (corresponding to the length of the Gamma catalog) are then extracted from the uniform distribution ranging between 0 and 1 randomly and the corresponding value in the cumulative curves is found (Figure 3.1). The synthetic catalog created by this extraction has sources with random latitude and longitude positions. The process is repeated until 1000 such synthetic catalogs are created. The distribution of the real Gamma catalog and one of the synthetic catalog is shown in Figure 3.2. This ensures that the simulated data conserved the shape of the modelling. Simulated catalogs also undergo the matching algorithm.

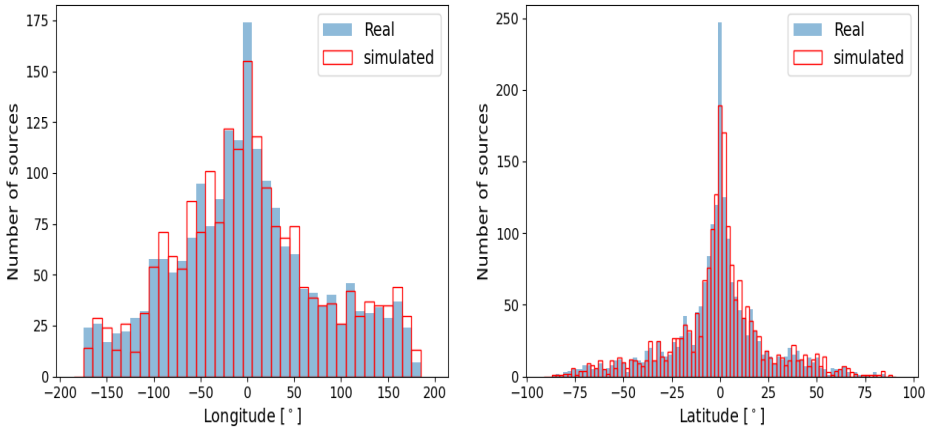

Figure 3.2: Distribution of longitude and latitude of one of the simulated catalogs compared to distribution of the Gamma catalog data

3.3 Significance of correlation

The number of matches in a simulated catalog are averaged to get an idea of mean number of matches over the entire collection of simulated catalogs. The distribution of number of matches of real and simulated data catalog is studied. For calculating the significance of the matches, the difference between number of matched sources with the real catalog (n_r) and mean of the number of matched sources with the synthetic catalog (n_s) is divided by the standard deviation (σ) of the distribution of number of matches of the synthetic catalog.

$$Significance, S = \frac{n_r - n_s}{\sigma}$$

If the significance is found to be greater than 3 (S $>$ 3), a correlation between the SC data and Gamma source is considered significant.

3.4 Results of matching

The matching and simulation described above is applied to both the SC catalogs. The star clusters used for this study is taken from Gaia catalog (refer to section 2.1.2) containing sources observed in optical - Near IR regime and from WISE catalog (refer to section 2.2.2) for the IR regime.

3.4.1 Matching with Gaia Catalog data

The Gaia catalog sources are divided into three age groups (refer section 2.1.2) based on the process that could be responsible for CR acceleration. The star cluster radius is given by the angular radius that contains 50% of the cluster members in the Gaia catalog. Each of sources are matched with the sources in the Gamma catalog using the matching algorithm described in section 3.1. If the angular distance is less than the angular radius of the star cluster, the γ-ray source in the Gamma catalog is overlapping with the Gaia sources and is said to be matched source. The sources in each age group are also matched with the sources in 1000 simulated catalogs (refer section 3.2). The mean number of matched sources is calculated for each synthetic catalog. Then the significance of the matches is found (refer section 3.3).

Group 1

Group 1 sources have age less than 3 Myr and the energy to accelerate CR is provided by stellar wind. At these ages, the supernova has not started exploded yet. There are 3 sources in the Gaia catalog that comes under this age classification.

These sources are matched with the real Gamma catalog. The sources in Group 1 do not have any matches with the Gamma catalog sources (Table 3.1). This means that no unidentified γ-ray sources are overlapping with the star clusters observed by Gaia telescope which has an age less than 3 Myr.

Group	Total no. of sources	Total number of sources matched with unidentified Gamma sources
Group 1	3	0
Group 2	1379	87
Group 3	5785	291

Table 3.1: Number of matched sources in the Gamma catalog with various age groups of star clusters in the Gaia catalog

Group 2

Group 2 contains Gaia sources with age between 3 Myr and 35 Myr. These star clusters have both stellar wind and supernova explosions that could provide energy to accelarate CR. To study if these sources are possible γ-ray emitters, the matching algorithm was done between these sources and sources in Gamma catalog. Out of the 1379 sources of Gaia catalog in Group 2, 87 sources have a match with sources in

the Gamma catalog. These 87 star clusters in Gaia have matched with 250 sources in the Gamma catalog (Figure 3.3) . Out of these, 31 star clusters have more than one Gamma sources that satisfy the matching conditions. To verify if this correlation is random or not, the sources in Group 2 were also matched with synthetic catalogs.

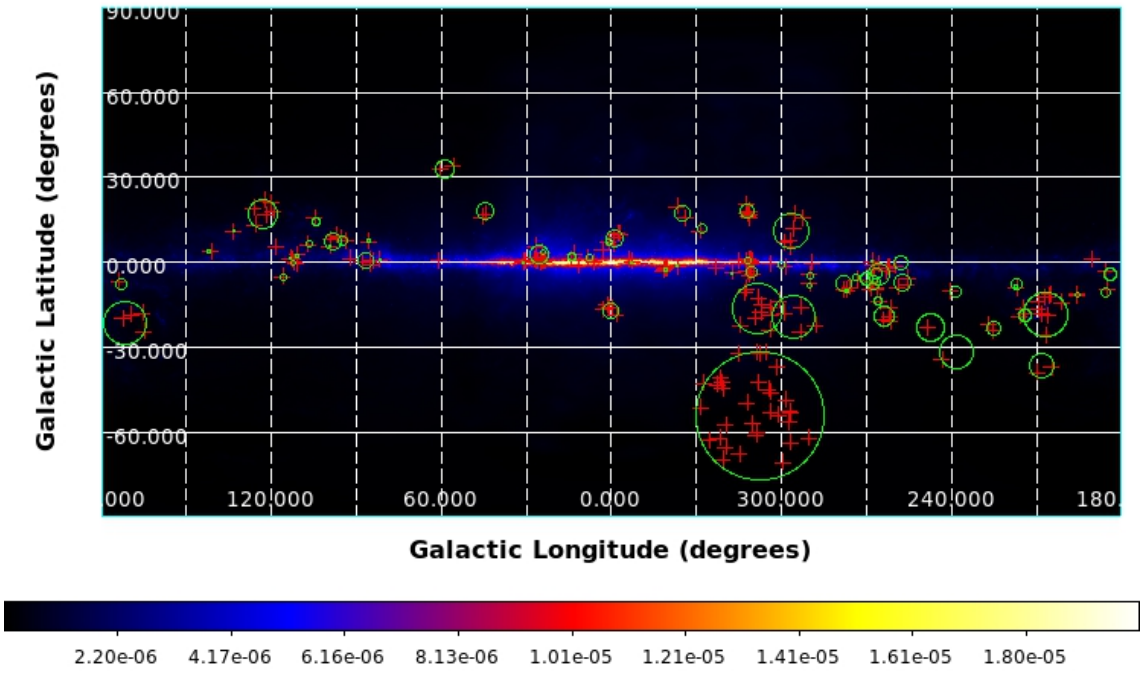

Figure 3.3: Illustration of Group 2 sources that matched with Gamma sources plotted over the Galactic interstellar diffuse emission model is gll iem v07. Matched Group 2 sources are given in green circles and matched Gamma sources are given in red crosses

Each of the 1000 synthetic catalogs obtained through the simulations (refer section 3.2) were matched with star clusters in Group 2. After this, the number of matched sources is averaged for each synthetic catalog. In average 74.343 star clusters in Group 2 were matched with 217.562 synthetic catalog sources. The distribution of number of Gaia source matches is plotted in Figure 3.5a. The distribution of number of matches for synthetic catalog has a standard deviation of 6.34. The green vertical line represents the number of Gaia sources in Group 2 matched with the Gamma catalog (87 sources) and the blue vertical line represents average number of the Gaia sources in Group 2 matched with the simulated catalog (74.343 sources). The significance (refer section 3.3) is calculated to be less than 3 ($S = 1.99$), therefore a clear conclusion on the randomness of the correlation cannot be established between the matches with the real catalog.

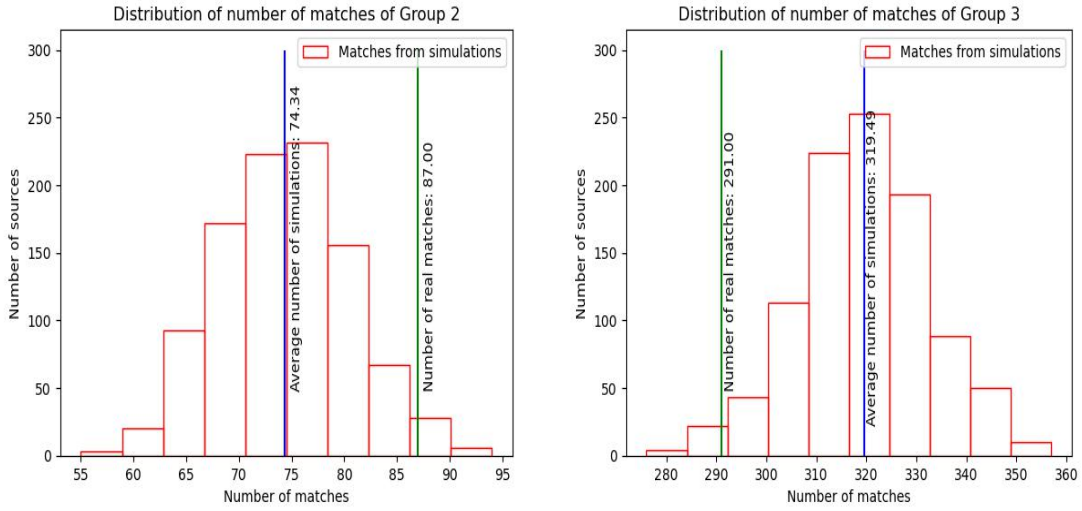

Figure 3.4: Distribution of average number of matches of sources in Gaia catalog with synthetic catalog. Green vertical line represents the number of Gaia sources matched with the Gamma catalog and the blue vertical line represents average number of the Gaia sources matched with the synthetic catalog Left: Distribution of number of matches for Group 2, Right: Distribution of matches for Group 3

Group 3

The Group 3 contains sources in the Gaia catalog having age greater than 35 Myr. At this time, the contribution of the stellar wind is negligible and the energy is given by supernova explosions for the acceleration of CR. The matching algorithm was applied to these star clusters and sources in the Gamma catalog. Out of 5785 sources in Group 3, 291 sources have one or more matches with the sources in the Gamma catalog. These are matched with 1112 sources in the Gamma catalog (Figure 3.5). 112 star clusters in Group 3 overlap with more than one γ-ray source from the Gamma catalog.

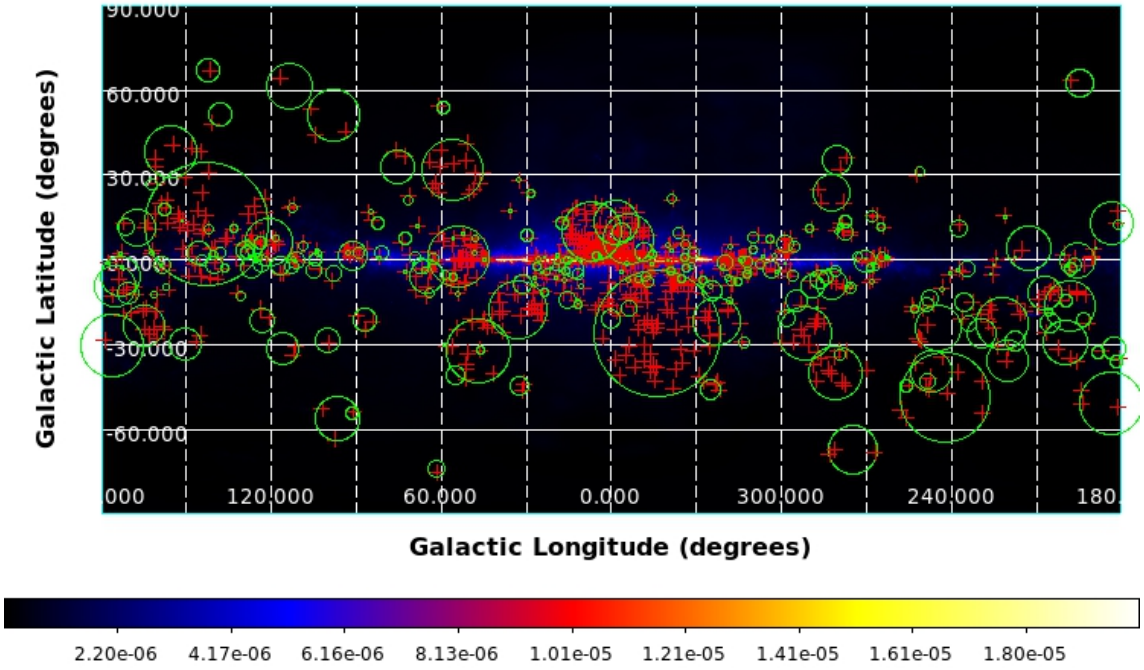

Figure 3.5: Illustration of Group 3 sources that matched with Gamma sources plotted over the Galactic interstellar diffuse emission model is gll iem v07. Matched Group 3 sources are given in green circles and matched Gamma sources are given in red crosses

The sources in 1000 synthetic simulated catalogs are matched with each star cluster in Group 3. After this, the number of matched sources is averaged for each synthetic catalog. For Group 3 sources, in average, 319.491 star clusters are matched with an average of 1196.887 synthetic catalog sources. The distribution number of Gaia source matches with the synthetic catalog is plotted as a histogram as seen in Figure 3.5b. The distribution of number of matches for synthetic catalog has a standard deviation (σ) of 12.83. The green vertical line represents the Gaia sources matched with the Gamma catalog (291 sources) and the blue vertical line represents average number of the Gaia sources matched with the simulated catalog (319.491 sources). The significance is calculated (refer to section 3.3) to be less than 3 (S=2.22), therefore a clear conclusion on the randomness of the correlation cannot be established between the matches.

3.4.2 Matching with WISE catalog data

The WISE catalog (refer section 2.2.2) contains sources of IR radiation from HII regions. Star clusters with age less than 1 Myr are obscured by the HII cloud. These clusters are thought to accelerate CR by stellar winds. Due to the obscuration, the star clusters are observed in the IR in the 12 and 22 micron by WISE satellite. The angular radius is given in arc seconds which is converted to degrees for this study.

The sources in the WISE catalog is matched with the sources in the Gamma catalog using the matching algorithm. Out of 8412 sources, 101 sources in the WISE catalog has a match with one or more source in the Gamma catalog (Figure 3.6). These sources match with 123 sources in the Gamma catalog. 18 WISE sources have more than one matches with the sources in Gamma catalog.

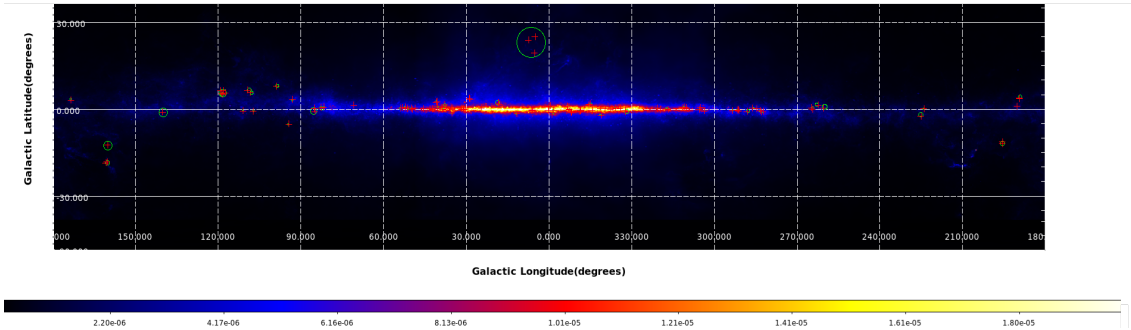

Figure 3.6: Illustration of WISE sources that matched with Gamma sources plotted over the Galactic interstellar diffuse emission model is gll iem v07. Matched WISE sources are given in green circles and matched Gamma sources are given in red crosses

The matching algorithm was applied to the sources in the 1000 synthetic catalogs. With the synthetic catalogs, the average number of WISE source matches was 42.134 to an average of 53.118 sources in Gamma catalog. The distribution of average number of WISE source matches with the synthetic catalog is plotted (Figure 3.7). The distribution of number of matches for synthetic catalog has a standard deviation (σ) of 6.4. The green vertical line represents the WISE sources matched with the Gamma catalog (101 sources) and the blue vertical line represents average number of the WISE sources matched with the simulated catalog (42.134 sources in average)

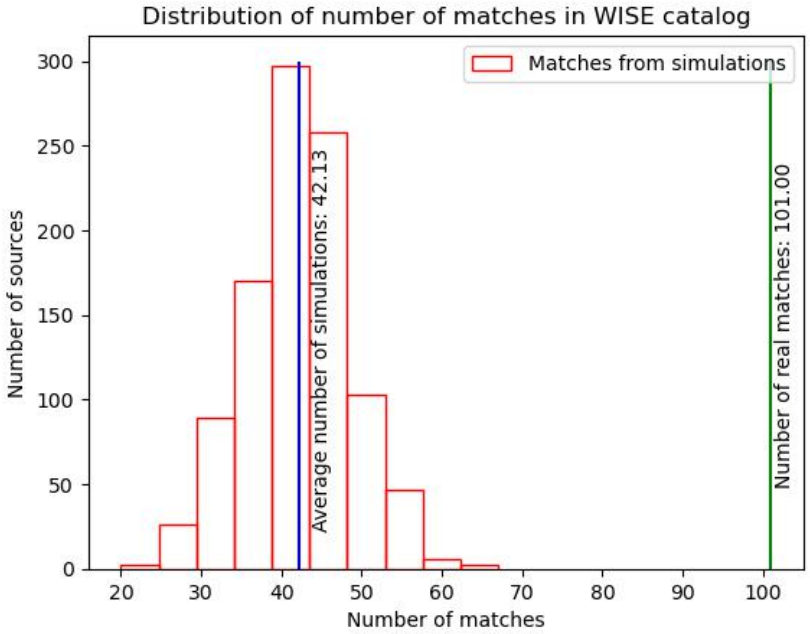

Figure 3.7: Comparision between the number of sources in the real and synthetic catalog matching with the Gamma catalog. The green line represents the number of WISE sources matching with Gamma catalog and blue represents mean number of WISE sources matching with simulated catalog

The significance is calculated to be greater than 3 (S = 9.15), suggesting that the correlation between the matches between the catalog sources are not random. The high spatial correlation of the matches between the sources are seen. These

matches are subjected to further analysis to study their characteristics in the next section.

Chapter 4

Fermi analysis and Results

4.1 Fermi analysis

In the first section of this study, 101 WISE catalog sources have been found to have association with one or more sources in the Gamma catalog. Out of these, three Gamma sources that are matching with WISE sources are selected for further analysis using the Fermi-LAT analysis tools.

The Fermi-LAT data are selected for a region of interest (RoI) centered on the coordinates of the sources of interest. Then a source model that contains the information about the spatial and spectral parameters is fitted to the data. The Fermi-LAT analysis package Fermipy convolves the emission of each source with the instrument response function (IRF) in order to predict the number of observed counts (refer Fermi analysis).

4.1.1 Source selection

The WISE sources that matched with sources in the Gamma catalog in section 3.3.2 are considered. These WISE sources are matched with identified sources in the Fermi-LAT DR3 catalog. These WISE sources are then removed from the matched sources. The remaining 87 WISE sources are then subject to the following selection criteria:

- They should have only one match with the source in Gamma catalog.
- They should have a calculated 22 micron flux value (given by the 'WISE $22um < br > (Jy)$' column in the WISE catalog)
- They should have a calculated distance value (given by the 'Dist.$< br >$(kpc)' column in WISE catalog).

Out of the total 101 matched WISE sources, 9 WISE sources satisfy the above criteria. The 22 micron flux of these WISE sources are checked and 3 WISE sources given in which have high, medium and low comparative fluxes are selected (Figure 4.1). The sources in the Gamma catalog that correspond to these WISE sources are selected for further analysis using Fermi analysis tools.

The Fermi sources (Table 4.3) that coincide with WISE sources (Tables 4.2) selected for the analysis. These γ-ray sources are subject to the Fermi analysis (refer section 4.1).

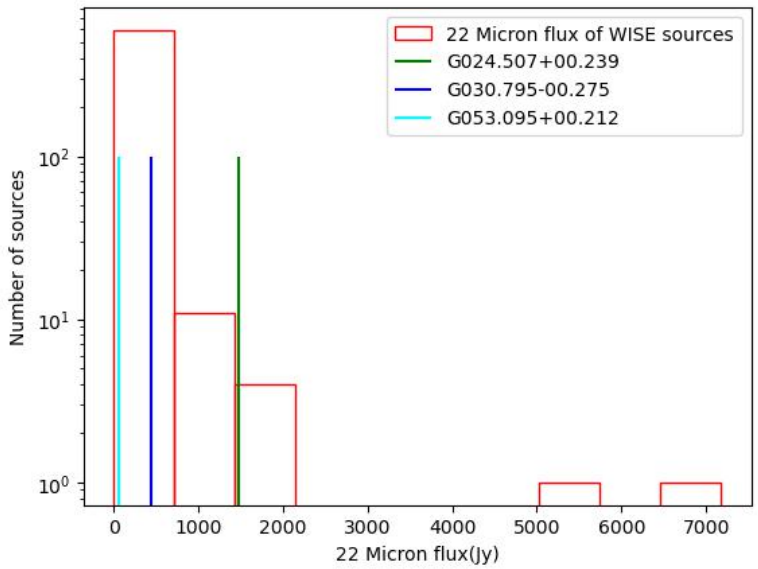

Figure 4.1: 22 Micron Flux of selected WISE sources compared to Matched WISE sources (refer section 3.2.2). The selected WISE sources (given in Table 4.2) are highlighted as vertical lines. Low flux in cyan (G053.095+00.212), medium flux in blue (G030.795-00.275), and high flux in green (G024.507+00.239)

Name	Glong (deg)	Glat (deg)	Radius (degrees)	Distance (kpc)	22-micron flux (Jy)
G024.507+00.239	24.508	0.24	0.1025	8.8	1481.85
G030.795-00.275	30.795	-0.275	0.0844	7.3	440.47
G053.095+00.212	53.095	0.212	0.0892	10.3	62.72

Table 4.1: WISE sources that were selected for further analysis. These sources satisfy the source selection criteria in Section 4.1.1.

The Fermi sources $4FGLJ1834.7-0724c$, $4FGLJ1848.6-0202c$, $4FGLJ1928.4+1801c$, are selected for further analysis. These sources have a single counterpart in the IR regime per the first section of these study.

Name	original longitude (deg)	original latitude (deg)
4FGL J1834.7-0724c	24.434818	0.3115942
4FGL J1848.6-0202c	30.791918	-0.31746978
4FGL J1928.4+1801c	53.11527	0.28535038

Table 4.2: Unidentified γ-ray sources are selected for Fermi analysis from the Gamma catalog that show association with the selected WISE sources in Table 4.1.

4.1.2 Starting Model

The data is extracted from the Fermi-LAT data server. The primary data files or event files contain records of discrete events as well as the reconstructed direction and energy for each event. The spacecraft file contains all information about the position and orientation of the Fermi-LAT spacecraft provided at 30 second intervals. Data is reduced by using the data combined with the spacecraft file.

The data for this work collected between from August 4th, 2008 to July 9th 2023 with energy range 100 MeV to 500 GeV. The search radius is 25 degrees centered around 284.27° right ascension and 3.29° declination (Table 4.3). The centroid of this search circle is selected such that it contains all the selected γ-ray sources given in Table 4.1. The spacecraft data was also downloaded along with the photon data files.

Equatorial coordinates (degrees)	(284.265,3.28927)
Time range (MET)	(239557417,710600254)
Time range (Gregorian)	(2008-08-04 15:43:36,2023-07-09 12:57:29)
Energy range (MeV)	(100,500000)
Search radius (degrees)	25

Table 4.3: Selection criteria for data extracted from Fermi-LAT with a 25 degree radius around centroid that contains all selected Gamma sources

Galactic diffuse emission model accounts for the diffuse background contribution from galactic sources (including pion decay, inverse compton and bremmstrahlung emissions). The isotropic diffuse emission model takes into account for the background contribution from extra-galactic diffuse γ-rays, unresolved extra-galactic sources, and residual cosmic-ray emission.

Here, the Galactic Interstellar diffuse emission model is *gll_iem _v07* with the corresponding isotropic diffuse emission spectral template *iso_P8R3 _SOURCE_V3 _v1*.

The data were taken from Pass 8 (P8R3) LAT data. The instrument response function (IRF) contains the reconstruction/simulation parameters used to generate an event class (*P8R3_SOURCE _V3*). The data was subjected to selection cuts as explained below.

4.1.3 Selection cuts

The following selection cuts were applied to the Fermi-LAT data.

- Select SOURCE class events by including only events with high probability of being photons (*evtclass*=128).
- Event type can help to select events based on the conversion type, track reconstruction and energy measurement. Select all event types(*evtype* = 3).
- Select only data with maximum zenith value equals 90 degrees to avoid residual contamination from Earth's limb.
- Select only the Good Time Intervals (GTI) where the data quality is optimal (DATA _QUAL > 0).
- Select data when the Fermi LAT was in standard data taking mode (LAT_CONFIG = 1).

For each selected source, a region of interest (ROI) width of $8^\circ \times 8^\circ$ is selected. The energy is binned into 30 uniform logarithmic bins with size equal to 0.2 degrees.

The Fermi LAT analysis is as follows:

- The **gtbin** tool is used to bin the event data according to their position and/or energy. This creates a counts map with a given number of energy slices separated by given bin size of 0.2 degrees in the ROI. The CMAP produces a single two-dimensional spatial count map whereas CCUBE creates 3D maps (2 spatial + one energy).
- The **gtexpcube2** tool creates an exposure map that accounts for the contribution of exposure of the entire sky. Here $360^\circ \times 180^\circ$ number of pixels is given for a bin size of 1 degrees.
- The **gtsrcmaps** tool creates source model maps by taking each source spectrum of the sources in the source model. Then it multiplies each model map by the exposure at the source position, and convolves that exposure with the effective PSF.

In order to find the best fit model parameters a likelihood analysis is implemented as described below.

4.1.4 Likelihood analysis

The likelihood L is the probability of obtaining a particular data given an input model. Each of the γ-ray sources in the RoI is described as a set of spatial component (Coordinates of position and shape of the source) and spectral component (model for energy distribution). For Poissonian distribution, the probability of observing 'n_i' number of counts in each bin 'i' is given by Eq. 4.1.

$$P_i(n_i) = \frac{\lambda_i^{n_i}}{n_i!} e^{-\lambda_i} \tag{4.1}$$

where the expected counts in the i^{th} bin is given by λ_i.

The Likelihood is calculated as a product of probability of observing the number of detected counts in each bin (Eq. 4.2).

$$L = \prod_i P_i(n_i) = e^{-N_{exp}} \prod_i \frac{\lambda_i^{n_i}}{n_i!} \tag{4.2}$$

Here N_{exp} is the total number of expected counts from the source model. Log-likelihood ($\mathcal{L}$) is more commonly used in Fermi analysis described as below (Eq. 4.3).

$$\mathcal{L} = -2logL = 2N_{exp} - 2\prod_i \left(\frac{\lambda_i^{n_i}}{n_i!}\right) \tag{4.3}$$

The fitting algorithm optimizes the fits over a finite number of iterations and gives the parameters that has the maximum loglikelihood value. A binned maximum likelihood analysis was used as the optimization technique with the optimizer ' NEWMINUIT ' for this study.

4.1.5 Residual investigation

The Test Statistic gives an idea of the goodness of the fit of the model over another. It is calculated as the maximum likelihood test statistic ($\mathcal{L}$) for each spatial bin as twice the log-like difference between null hypothesis and other models (Eq. 4.4).

$$TS = 2log\left(\frac{\mathcal{L}_{new\ model}}{\mathcal{L}_{null\ model}}\right) \tag{4.4}$$

The TS value gives the significance (σ) of the source (Eq. 4.5).

$$\sigma = \sqrt{TS} \tag{4.5}$$

4.1.6 Spatial and Spectral modelling

The alternative spatial models given below are used to study in the maximum log-likelihood fitting method.

- The null hypothesis assumed that the real source doesn't exist and has no significance to the set of observations.
- A new point source at the position of the original source with a 'power law' spectral type.
- Two new point source at the position of the original source with a 'power law' spectral type.
- A new extended source at the alternate position with a 'power law' spectral type and 'RadialDisk' model type.

To find the parameters for the extended source spatial model, a source extension test is done for the selected source using the **extension** tool as decribed below.

Extension fit

The source is fitted with an extension that maximizes the log-likelihood after performing a likelihood scan over the source width. The position of the best fit model and extension is substituted in the spatial modelling for extended source. To find the best fitting spatial model, the following test is done.

Akaike Information Criterion (AIC) test

The Akaike Information Criterion (AIC) test is performed to find the best fitting spatial model. The AIC evaluates how well a model fits the data. It is calculated from using the Eq. 4.6.

$$AIC = -2ln\left(\mathcal{L}\right) + 2k \tag{4.6}$$

where $\mathcal{L}$ is the log-likelihood given by the fit and k is the number of independent parameters for the model. To compare AIC between the null hypothesis and 1 point source the the difference of free parameters is given by $\Delta k = 2$. The AIC for 2 point sources ($\Delta k = 4$) and extended source ($\Delta k = 3$) is also compared against AIC of the null hypothesis. It was found that the fit using the extended source had the lowest AIC score difference for all sources (Appendix A). The extended source is considered as a better fit model over the superposition of 2 separate point sources if,

$$AIC_{extended} < AIC_{2points}$$

Spectral energy distribution (SED) analysis

The model is optimized to get minimum residuals from the TS map (Additional sources are added in case to minimize the residual if needed, refer Appendix B) and morphology is also tested. The spectral energy distribution (SED) was computed for the source using the **sed** tool of fermipy and an output file containing the information about energy bins, energy, differential flux, log-likelihood for best-fit amplitude etc is generated. The **sed** tool divides the flux into energy bins with flux normalizations in each bin fitted with a power-law spectral parameterization with a fixed index.

Curvature test

A curvature test is done to determine the best spectral type for the source. This is done with the **curvature** tool of fermipy. This tool tests the different spectral models for best description of the given data.

- Powerlaw (PL):

  The first spectral model is the simple Powerlaw (defined by Eq. 4.7). Here the differential photon flux is proportional to the function of energy of photons powered to the spectral index (Γ). Here E_0 is the normalization energy. N_0 is the normalization flux at E_0.

$$\frac{dN}{dE} = N_0 \left(\frac{E}{E_0}\right)^{\Gamma} \tag{4.7}$$

- Log-Parabola (LP) :

  The second spectral model is the Log Parabola (defined by Eq. 4.8). The difference between the simple Powerlaw and Log Parabola is the extra curvature term β. This can describe the curvature on either sides of the peak of the SED, covering a wide range of energies than a simple powerlaw.

$$\frac{dN}{dE} = N_0 \left(\frac{E}{E_0} \right)^{-\Gamma - \beta\, ln(\frac{E}{E_0})} \tag{4.8}$$

- Powerlaw with super exponential cutoff (PLSuperExpCutoff4):

  Here the Powerlaw spectrum has a super-exponential cutoff (defined by Eq. 4.9). The factor d is the local curvature at E_0. Γ_0 is the spectral index at E_0 and b is the spectral index at the exponential part of the spectra. In general, b is taken as a constant value 0.6667 for the curvature test. Since $b > 0$, the model behaves as a powerlaw at low energies and it decreases exponentially toward high energies. If b=0, the spectral model becomes a log parabola with $\Gamma = \Gamma_0$ and $\beta = \mathrm{d}/2$.

$$\frac{dN}{dE} = N_0 \begin{cases} \left(\frac{E}{E_0}\right)^{\Gamma_0 - \frac{d}{2} ln(\frac{E}{E_0}) - \frac{db}{6} ln^2(\frac{E}{E_0}) - \frac{db}{24}^2 ln^3(\frac{E}{E_0})} & , if\ |b\, ln(\frac{E}{E_0})| < 1e^{-2} \\ \left(\frac{E}{E_0}\right)^{\left(\Gamma_0 + \frac{d}{b}\right)}\ exp(\frac{d}{b^2}(1 - (\frac{E}{E_0})^b)) & , \text{otherwise} \end{cases} \tag{4.9}$$

The **curvature** tool in fermipy compares the log-likelihood of different spectral models for a given source. Here the tool compares the log-likelihood ratio between spectral models Power law, Log Parabola, Power law with a super exponential cutoff (Eq. 4.10-4.11).

$$TS_{LP} = -2\,(lnL_{PL} - lnL_{LP}) \tag{4.10}$$

$$TS_{PLSuperExpCutoff4} = -2\,(lnL_{PL} - lnL_{PLSuperExpCutoff4}) \tag{4.11}$$

The tool returns the likelihood values for each spectral fit. The best fit is determined by maximum likelihood value between the spectral fits.

4.2 Results of Fermi analysis of selected sources

Gamma Source	new longitude (deg)	new latitude (deg)	extension (deg)
4FGL J1834.7-0724c	24.4462 ± 0.0300	0.1883 ± 0.0272	$0.2363^{+0.0435}_{-0.0435}$
4FGL J1848.6-0202c	30.7907 ± 0.0302	-0.2760 ± 0.0271	$0.5314^{+0.0327}_{-0.0377}$
4FGL J1928.4+1801c	52.9729 ± 0.1804	0.1168 ± 0.0461	$0.8628^{+0.0732}_{-0.0795}$

Table 4.4: Position and extension of selected Gamma sources after extension test. The position is shifted from the original position of the Gamma source and the Gamma source shows an extended spatial profile rather than a point source profile

4.2.1 Source 4FGL J1834.7-0724c

The source 4FGL J1834.7-0724c is matched to the WISE source G024.507+00.239. It has a radius of 369 arcseconds positioned at a distance 8.8 kpc from Earth as indicated by the respective source in the WISE catalog. It has a high flux of 1481.85 Jy when compared to that of other matched sources in the WISE catalog (Figure 4.1). The count map of the Gamma source is created by the **gtbin** tool (Figure 4.2a).

The AIC test revealed that the Gamma source is best fitted with an extended source (see Appendix A) with an extension of 0.2363 degrees with a position shift from the original Gamma source position (Table 4.4). Some additional sources were added to improve the model (see Appendix B). TS map shows no sources with ts value greater than 9 (Figure 4.2b). This means all the remaining sources in the residue map have less than 3σ significance. After the curvature study, the best spectral model for SED (Figure 4.2c) is determined to be Power law with a super exponential cutoff (PLSuperExpCutoff4). The γ-ray flux from SED analysis is $3.36 \times 10^{-5}\, erg/cm^2 s$ and the spectrum extends to 10 GeV before cutoff.

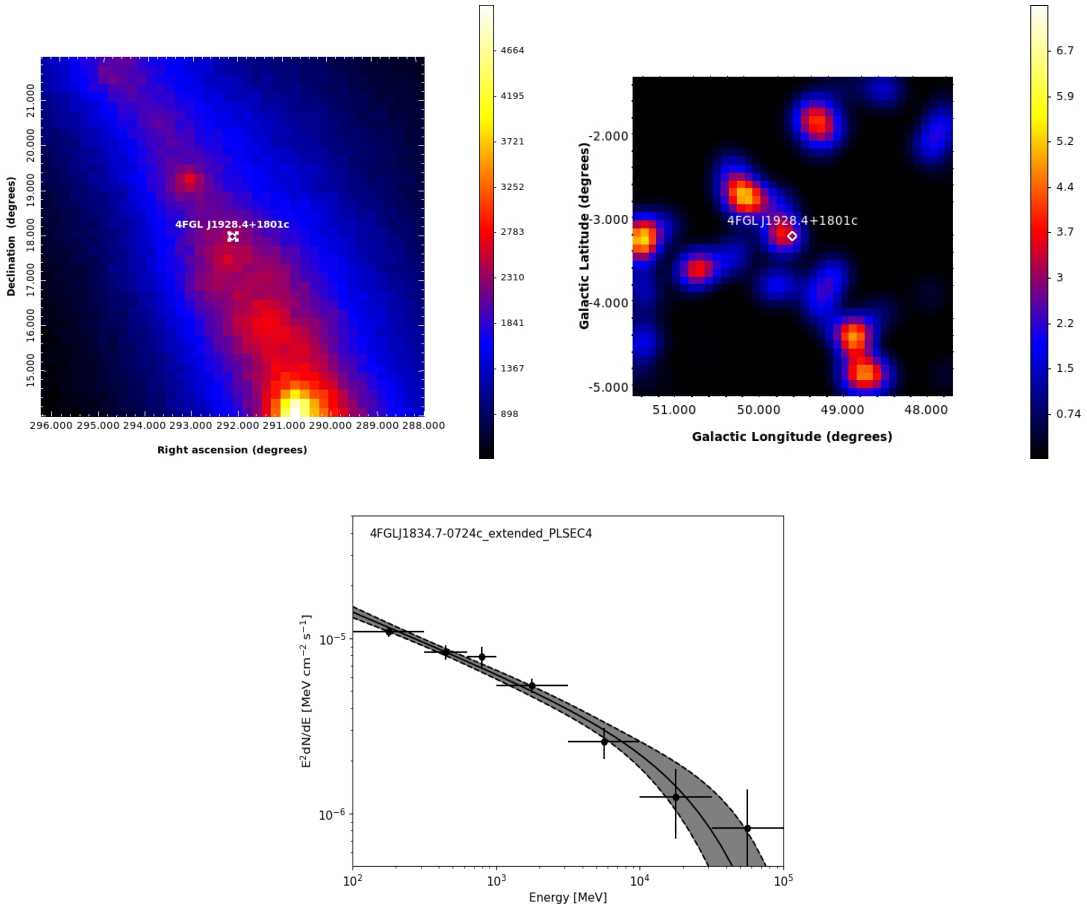

Figure 4.2: Results for the source 4FGL J1834.7-0724c. Top left panel: Counts map with the position of the Gamma source plotted in white circle. The colorbar signifies the number of counts observed. Top right panel: Residue map after fitting with an extended source model with a PLSuperExpCutoff4 spectral model. The color bar indicates the TS value (square of the significance) and the position of Gamma source given in white circles. Bottom panel: SED of the source fitted with a PLSuperExpCutoff4 spectral model with energy ranging from 100 MeV to 500 GeV.

4.2.2 Source 4FGL J1848.6-0202c

The source 4FGL J1848.6-0202c was matched to the WISE source G030.795-00.275. It has a radius of 304 arcseconds positioned at a distance 7.3 kpc from Earth as indicated by the respective source in the WISE catalog. It has a medium flux of 440.47 Jy when compared to that of other matched sources in the WISE catalog (Figure 4.1). The count map of the Gamma source is created by the **gtbin** tool (Figure 4.3a).

The AIC test revealed that the Gamma source is best fitted with an extended source (see Appendix A) with an extension of 0.5314 degrees with a position shift from the original Gamma source position (Table 4.4). Some additional sources were added to improve the model (see Appendix B). Residue map shows no sources with significance greater that 3σ (Figure 4.3b). After the curvature study, the best spectral model for SED (Figure 4.3c) is determined to be Power law with a super exponential cutoff (PLSuperExpCutoff4). The γ-ray flux from SED analysis is $5.40 \times 10^{-5}\, erg/cm^2 s$ and the spectrum extends to 10 GeV before cutoff.

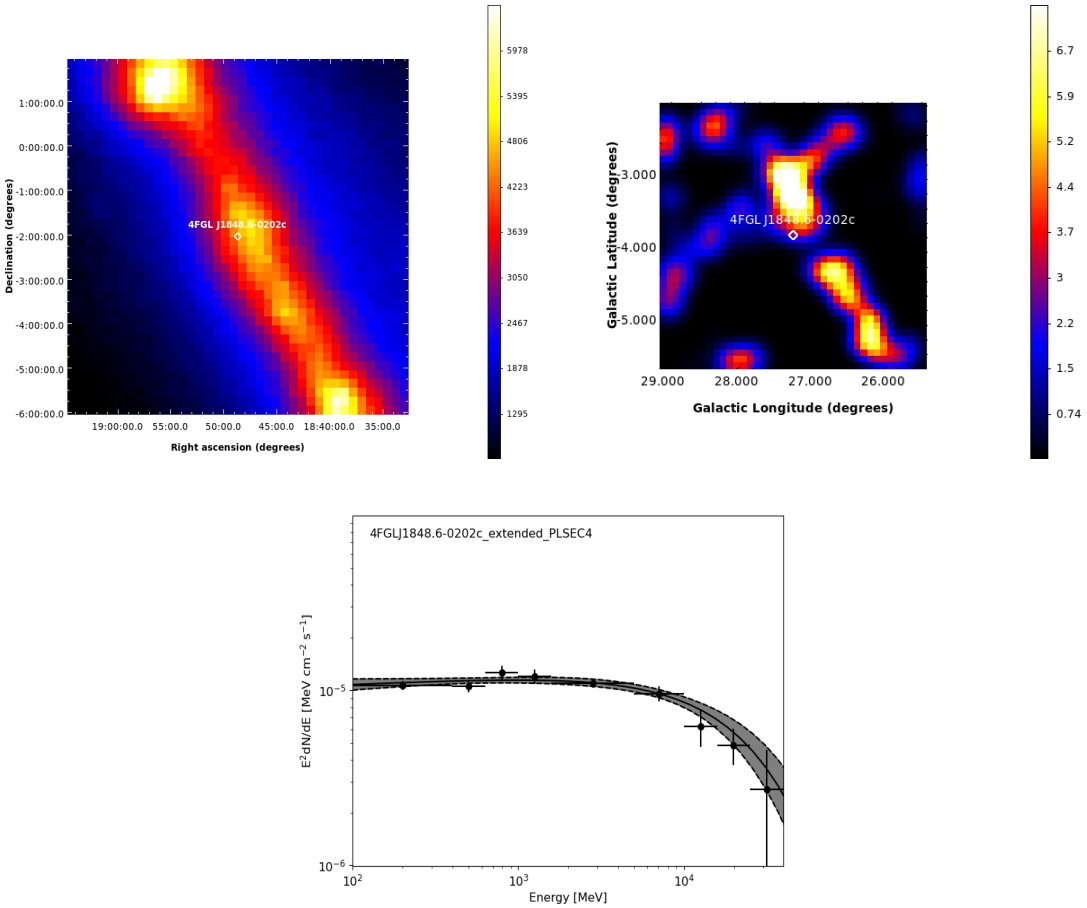

Figure 4.3: Results for the source 4FGL J1848.6-0202c. Top left panel: Counts map with the position of the Gamma source plotted in white circle. The colorbar signifies the number of counts observed. Top right panel: Residue map after fitting with an extended source model with a PLSuperExpCutoff4 spectral model. The color bar indicates the TS value (square of the significance) and the position of Gamma source given in white circles. Bottom panel: SED of the source fitted with a PLSuperExpCutoff4 spectral model with energy ranging from 100 MeV to 500 GeV.

4.2.3 Source 4FGL J1928.4+1801c

The source 4FGL J1928.4+1801c was matched to the WISE source G053.095+00.212. It has a radius of 321 arcseconds positioned at a distance 10.3 kpc from Earth as indicated by the respective source in the WISE catalog. It has a low flux of 62.72 Jy when compared to that of other matched sources in the WISE catalog (Figure 4.1). The count map of the Gamma source is created by the **gtbin** tool (Figure 4.4a).

The AIC test revealed that the Gamma source is best fitted with an extended source (see Appendix A) with an extension of 0.8628 degrees with a position shift from the original Gamma source position (Table 4.4). Some additional sources were added to improve the model (see Appendix B). Residue map shows no sources with significance greater that 3σ (Figure 4.4b). After the curvature study, the best spectral model for SED (Figure 4.4c) is determined to be Log Parabola (LogParabola). An alternative spectral model can be a simple power law for this source (both log parabola and power law model have similar log-like values). The γ-ray flux from SED analysis is $1.51 \times 10^{-5}\, erg/cm^2 s$ and the spectrum extends to 10 GeV without

any cutoff.

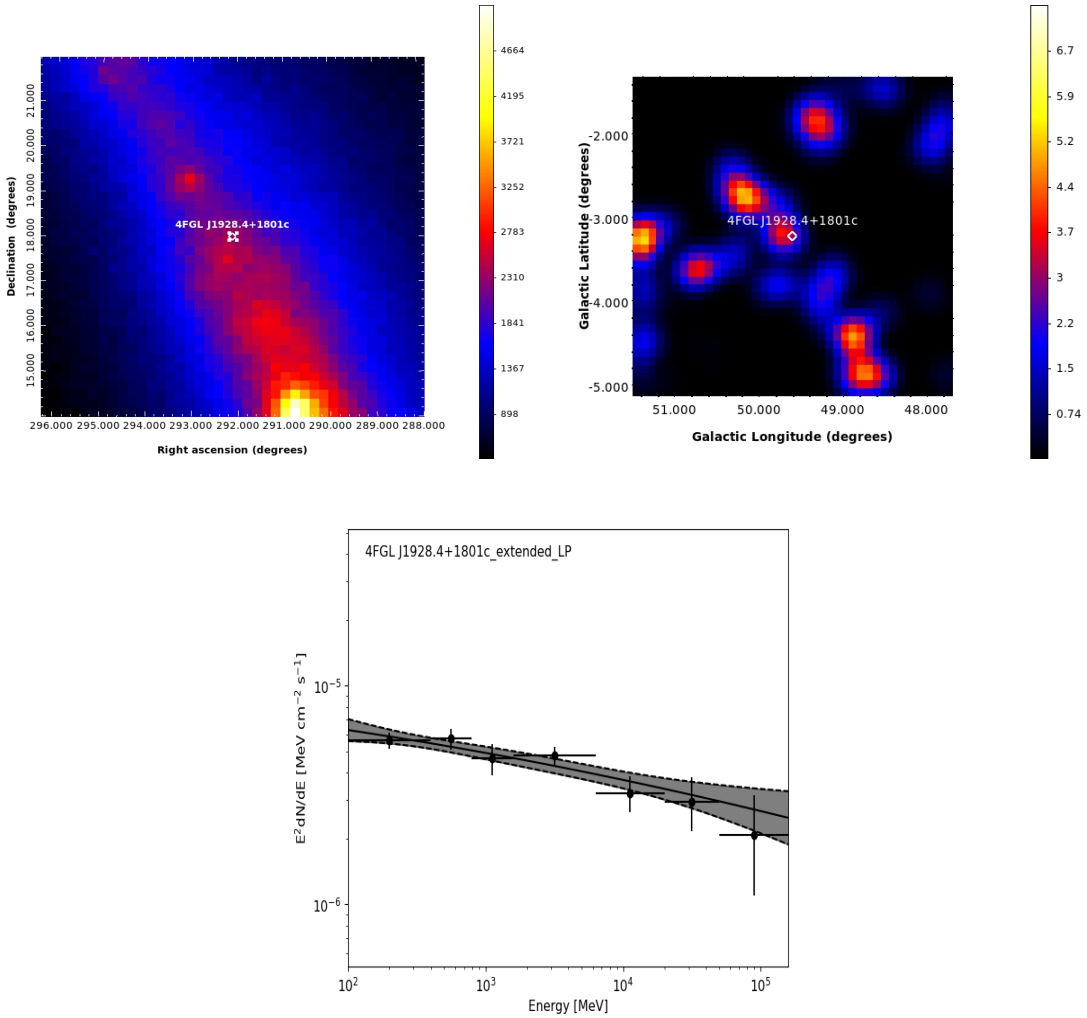

Figure 4.4: Results for the source 4FGL J1928.4+1801c. Top left panel: Counts map with the position of the Gamma source plotted in white circle. The colorbar signifies the number of counts observed. Top right panel: Residue map after fitting with an extended source model with a Log Parabola spectral model. The color bar indicates the TS value (square of the significance) and the position of Gamma source given in white circles. Bottom panel: SED of the source fitted with a Log Parabola spectral model with energy ranging from 100 MeV to 500 GeV.

After the spectral and energy characteristics of the chosen sources are studied using SED analysis, a further study on the luminosity of the chosen sources are done in the next section. Various luminosity of the sources are calculated from the SED and catalog data.

4.3 Luminosity

The integrated flux can be computed by multiplying the energy with differential flux ($\frac{dn}{dEdtdA}$) and integrating it (see Eq. 4.12).

$$F = \int E \frac{dn}{dE * dt * dA} dE erg/cm^2/s \tag{4.12}$$

The Gamma ray Luminosity (L_γ) is calculated from the flux using Eq 4.13, where the distance is taken from the SC catalog.

$$L_\gamma = F \times 4\pi d^2 \, erg/s \tag{4.13}$$

By assuming fast cooling (refer Section 1.5), i.e. all protons interact to produce γ-rays, the CR luminosity (L_{CR}) can be approximated to 3 times the gamma ray luminosity (L_{CR}=3×L_γ).

The mechanical luminosity or the stellar wind luminosity ($L_\star$) of the source can be calculated by assuming that the radius of γ-ray source is equal to the wind termination shock of the wind-blown bubble. This assumes that only the stellar wind from star cluster with age t, is responsible for the bubble expansion to a radius R in a medium of density n (Weaver et al 1977).

$$R = 27pc \left(\frac{\zeta L_*}{10^{36} erg/s} \right)^{1/5} \left(\frac{n}{1cm^{-3}} \right)^{-1/5} \left(\frac{t}{1Myr} \right)^{3/5} \tag{4.14}$$

$$L_* = \frac{10^{36} R^5 n t^{-2} \zeta^{-1}}{(27)^5} erg/s \tag{4.15}$$

The density is assumed to be that of a typical star forming region, $n \sim 1000 \, cm^{-3}$ and timescale as $t \sim$1 Myr. Radius R is the physical radius of the SC derived from the angular radius of the SC containing 50% of the cluster members and the distance given in the SC catalog. ζ is the fraction of wind luminosity that is used to inflate the bubble. From hydro dynamic simulations of young SC embedded in a dense medium, $\zeta = 0.0767$ (Yadav et al 2017).

The comparison of the CR luminosity L_{CR} to the mechanical luminosity L_* gives us the acceleration efficiency η of CR produced from the SC.

$$\eta = \frac{L_{CR}}{L_*} \tag{4.16}$$

In the IR band, the 22-micron flux from the WISE catalog is multiplied by the frequency to obtain the integrated flux, and then the IR luminosity (L_{IR}) is calculated using Eq. 4.13. The IR luminosity, γ-ray luminosity, CR luminosity and the stellar wind luminosity as calculated for our 3 sources are all reported in Table 4.5.

Source Name	4FGL J1834.7-0724c	4FGL J1848.6-0202c	4FGL J1928.4+1801c
IR Luminosity erg/s	18.7×10^{38}	3.83×10^{38}	1.09×10^{38}
Gamma ray Luminosity erg/s	$5.10 \pm 0.66 \times 10^{35}$	$5.51 \pm 0.56 \times 10^{35}$	$6.35 \pm 0.63 \times 10^{35}$
CR luminosity erg/s	1.54×10^{36}	1.65×10^{36}	1.91×10^{36}
Stellar wind luminosity erg/s	8.79×10^{38}	1.31×10^{38}	9.62×10^{38}

Table 4.5: Luminosity of selected sources in various methods. The IR luminosity of star cluster counterpart is calculated from the WISE catalog whereas the γ-ray lumnosity is calculated from the SED analysis of Gamma sources. The mechanical (stellar wind) luminosity is calculated by assuming a wind blown bubble around the Gamma source with radius comparable to the WISE source. The CR luminosity is calculated by assuming fast cooling of CR to produce γ-rays.

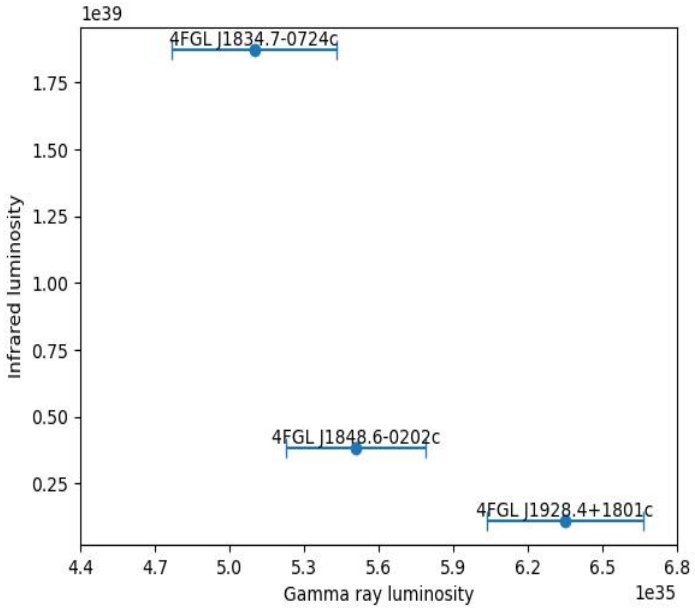

Figure 4.5: IR luminosity as a function of γ-ray luminosity for different sources with the error in γ-ray luminosity plotted as bars

The IR luminosity is plotted against the Gamma Ray luminosity in Fig.4.6. We notice that the 3 sources have similar Gamma Ray luminosites ($\sim 5 \times 10^{35}$ erg s^{-1}) but the IR luminosity is spread over $\sim$1 order of magnitude.

Source Name	4FGL J1834.7-0724c	4FGL J1848.6-0202c	4FGL J1928.4+1801c
$\frac{L_{CR}}{L_*}$	1.70×10^{-3}	12.6×10^{-3}	1.98×10^{-3}

Table 4.6: The calculated acceleration efficiency of selected sources by comparing the CR luminosity with the mechanical luminosity provided by stellar wind from the young star clusters.

The ratio of CR luminosity over the Stellar wind luminosity gives the efficiency of the CR acceleration. This ratio (given in Table 4.6) is approximately 0.1-1%. This means that the star cluster maybe able to provide this efficiency and the energetics are met for CR acceleration.

Chapter 5

Summary and Conclusion

The most promising candidate for the acceleration of Galactic cosmic rays have been considered to be Supernova Remnants. However, in recent years, some discrepancies in the SNR paradigm with observations (refer Chapter 1) has shifted the focus to the search of other possible astrophysical objects that may be able to accelerate CRs. One of the leading candidates under investigation currently are star clusters.

This thesis work focuses on the role of star clusters as CR accelerators by studying their γ-ray emission and properties. Given that star clusters are best selected in the optical and IR regime based on their evolution and age, the star cluster catalogs were selected from Gaia (in optical, 7167 Star clusters) and WISE (in the IR; 8412 SC). The unidentified sources in the Fermi catalog (1982 sources) were selected as a reference for γ-ray source catalog.

In Chapter 3, the first part of this work, a matching algorithm was applied to the Gaia catalog and WISE catalog sources separately to match them with the Unidentified Fermi sources (Gamma catalog). Starting from the Gamma catalog, 1000 synthetic catalogs were simulated, via Monte Carlo simulation, and matching algorithm was applied to each of them separately against the SC catalog.

The Gaia sources were separated into different age groups based on the age given in the Gaia catalog. This division is based on the fact that different ages have different components (stellar wind, supernova or both) that may contribute to the CR acceleration. The number of matches of real data is compared with the average number of matches with the simulated catalogs. The number of associations of Gaia SC with Gamma ray sources for all 3 Gaia sub-groups never reach the 3 σ significance when compared with the average of random associations. Hence a correlation between matches cannot be ascertained. The inconclusivity of Gaia source catalog matching to the unidentified Fermi sources could be due to the absence of ambient medium surrounding the star clusters, producing a lower γ-ray flux. Due to the limited collecting area and energy range of Fermi, these sources may not be detected at the moment.

When the sources in the WISE catalog were matched with Gamma catalog, a total of 101 WISE sources show association to 123 unidentified Fermi sources, as reported in Figure 3.6. The number of matched sources in the real catalog is compared to the average number of matched sources in the simulated catalogs. These matches have a significance of 9σ, which exceeds the average of random associations. This suggests there is a high spatial correlation between the matches of the WISE sources with the unidentified Fermi sources (almost 5 percent of the total Gamma catalog),

leading to the conclusion that these WISE sources are possible γ-ray emitters, and in turn could be CR accelerators.

In Chapter 4, second part of this work focus on further analysis of selected sources from the matched source in the Fermi-WISE catalog. Three sources, namely $4FGL\ J1834.7-0724c, 4FGL\ J1848.6-0202c, 4FGL\ J1928.4+1801c$, are selected for further analysis using Fermipy tools (refer Section 4.1). The associated WISE sources of these selected Fermi sources have low, medium and high detected 22 micron flux among the WISE SC catalog (see Fig. 4.1). These 3 Fermi sources were subjected to a binned likelihood analysis and a SED analysis in the energy range 100 MeV-500 GeV, and were modelled so that their TS map shows no sources with significance greater than 3.

SED analysis was used to study the individual luminosities in Section 4.3. The analysis studies showed extended spatial profiles for all selected sources. The energy and differential flux from the SED analysis was used to calculate the γ-ray luminosity with the distance taken from WISE catalog. The IR luminosity was calculated from the 22 micron flux from the WISE catalog. The CR luminosity is calculated as 3 times the value of γ-ray luminosity. The stellar wind luminosity (mechanical luminosity) is calculated by assuming only the contribution of stellar winds. The three analysed Fermi sources emit in γ-rays with a luminosity of the order of 10^{35} erg/s and in IR of the order of 10^{38} erg/s. The stellar wind luminosity has values of the order of 10^{38} erg/s, in the ranges of luminosities typically provided by stellar wind. The CR luminosity has values of the order of 10^{36} erg/s. The CR luminosity is 2 order of magnitude lower than the stellar wind luminosity. The efficiency is calculated as the CR luminosity over stellar luminosity (Table 4.5) and is in order of $10^{-3} - 10^{-2}$. The SED and Luminosity studies revealed that the CR luminosity is less than the mechanical luminosity and is around 0.1-1 percent of the mechanical luminosity.

The thesis started with the question of whether star cluster could be γ-ray emitters. The associations found by the matching between star clusters observed by WISE and unidentified sources observed by Fermi LAT in this work provide answer for this. The results suggest that the stellar winds of young star clusters (as they are observed in the IR spectrum) could provide ideal conditions to accelerate cosmic rays. At the end of this study, we can reach the conclusion that star clusters, especially younger ones, and the regions surrounding them, are ideal locations that could be serve as cosmic rays acceleration sites. Furthermore, this thesis work can be used to construct models for CR acceleration in star clusters and provide a comprehensive idea about the features such as acceleration efficiency. With future γ-ray telescopes like the Cherenkov Telescope Array Observatory (CTAO) and Southern Wide-field Gamma-ray Observatory (SWGO) with their large coverage area and energy range, it will become possible to further study the underlying features of these star clusters and their contribution to galactic CR acceleration.

Bibliography

Abdo A. A., et al., 2007, *TeV Gamma-Ray Sources from a Survey of the Galactic Plane with Milagro*,] 10.1086/520717

Abdo A. A., et al., 2010, *¡i¿FERMI¡/i¿ LARGE AREA TELESCOPE OBSERVATION OF A GAMMA-RAY SOURCE AT THE POSITION OF ETA CARINAE*, The Astrophysical Journal, 723, 649

Abdollahi S., et al., 2020, *¡i¿Fermi¡/i¿ Large Area Telescope Fourth Source Catalog*, The Astrophysical Journal Supplement Series, 247, 33

Abramowski A., et al., 2011, *Revisiting the Westerlund 2 field with the HESS telescope array*, Astronomy & Astrophysics, 525, A46

Acciari V. A., et al., 2011, *Discovery of TeV Gamma Ray Emission from Tycho's Supernova Remnant*,] 10.1088/2041-8205/730/2/L20

Ackermann M., et al., 2011, *A Cocoon of Freshly Accelerated Cosmic Rays Detected by Fermi in the Cygnus Superbubble*, Science, 334, 1103

Aharonian F., et al., 2007, *Detection of extended very-high-energy ¡i¿¡/i¿ -ray emission towards the young stellar cluster Westerlund 2*, Astronomy & Astrophysics, 467, 1075

Aharonian F., Yang R., de Oña Wilhelmi E., 2018, *Massive Stars as Major Factories of Galactic Cosmic Rays*

Aharonian F., et al., 2022, *A deep spectromorphological study of the γ-ray emission surrounding the young massive stellar cluster Westerlund 1*,] 10.1051/0004-6361/202244323

Amato E., 2014, *The origin of galactic cosmic rays*,] 10.1142/S0218271814300134

Anderson L. D., Bania T. M., Balser D. S., Cunningham V., Wenger T. V., Johnstone B. M., Armentrout W. P., 2014, *THE ¡i¿WISE¡/i¿ CATALOG OF GALACTIC H II REGIONS*, The Astrophysical Journal Supplement Series, 212, 1

Baade W., Zwicky F., 1934, *Remarks on Super-Novae and Cosmic Rays*, Physical Review, 46, 76

Bartoli B., et al., 2014, *IDENTIFICATION OF THE TeV GAMMA-RAY SOURCE ARGO J2031+4157 WITH THE CYGNUS COCOON*, The Astrophysical Journal, 790, 152

Bell A. R., 1978, *The acceleration of cosmic rays in shock fronts - I*, Monthly Notices of the Royal Astronomical Society, 182, 147

Bhadra S., Gupta S., Nath B. B., Sharma P., 2022, *Cosmic rays from massive star clusters : A close look at Westerlund 1*,] 10.1093/mnras/stac023

Blandford R. D., Ostriker J. P., 1978, *Particle acceleration by astrophysical shocks*, The Astrophysical Journal, 221, L29

Blasi P., 2013, *The Origin of Galactic Cosmic Rays*,] 10.1007/s00159-013-0070-7

Bykov A. M., Ellison D. C., Gladilin P. E., Osipov S. M., 2015, *Ultrahard spectra of PeV neutrinos from supernovae in compact star clusters*, Monthly Notices of the Royal Astronomical Society, 453, 113

Bykov A. M., Ellison D. C., Gladilin P. E., Osipov S. M., 2017, *Supernovae in compact star clusters as sources of high-energy cosmic rays and neutrinos*,] 10.1016/j.asr.2017.05.043

Bykov A. M., Marcowith A., Amato E., Kalyashova M. E., Kruijssen J. M. D., Waxman E., 2020, *High-energy particles and radiation in star-forming regions*,] 10.1007/s11214-020-00663-0

Collaboration H., Aharonian F., 2001, *Evidence for TeV gamma ray emission from Cassiopeia A*,] 10.1051/0004-6361:20010243

Collaboration H. E. S. S., : Aharonian F., 2004, *High-energy particle acceleration in the shell of a supernova remnant*,] 10.1038/nature02960

Collaboration F., : Atwood W. B., 2009, *The Large Area Telescope on the Fermi Gamma-ray Space Telescope Mission*,] 10.1088/0004-637X/697/2/1071

Collaboration H., et al., 2011, *Discovery of extended VHE -ray emission from the vicinity of the young massive stellar cluster Westerlund 1*,] 10.1051/0004-6361/201117928

Collaboration H. E. S. S., et al., 2014, $TeV\ \{\gamma\} - rayobservationsoftheyoungsynchrotron - dominatedSNRsG1.9 + 0.3andG330.2 + 1.0withH.E.S.S.$,]$10.1093/mnras/stu459$

Collaboration H. E. S. S., et al., 2015, *The exceptionally powerful TeV gamma-ray emitters in the Large Magellanic Cloud*,] 10.1126/science.1261313

Collaboration G., Brown A. G. A., Vallenari A., Prusti T., de Bruijne J., Mignard F., Drimmel R., co authors ., 2016, *Gaia Data Release 1. Summary of the astrometric, photometric, and survey properties*,] 10.1051/0004-6361/201629512

Cristofari P., 2021, *The Hunt for Pevatrons: The Case of Supernova Remnants*,] 10.3390/universe7090324

Engel R., Gaisser E. R. T., 2016, *Cosmic Rays and Particle Physics*. Cambridge University Press

Fermi E., 1954, *Galactic Magnetic Fields and the Origin of Cosmic Radiation.*, The Astrophysical Journal, 119, 1

Gabici S., 2022, *Low-energy cosmic rays: regulators of the dense interstellar medium*, The Astronomy and Astrophysics Review, 30, 4

Gabici S., 2023, *Cosmic rays from star clusters*

Gabici S., Evoli C., Gaggero D., Lipari P., Mertsch P., Orlando E., Strong A., Vittino A., 2019, *The origin of Galactic cosmic rays: challenges to the standard paradigm*,] 10.1142/S0218271819300222

Gupta S., Nath B. B., Sharma P., Eichler D., 2020, *Realistic modelling of wind and supernovae shocks in star clusters: addressing 22Ne/20Ne and other problems in Galactic cosmic rays*, Monthly Notices of the Royal Astronomical Society, 493, 3159

Higdon J. C., Lingenfelter R. E., 2003, *The Superbubble Origin of ¡sup¿22¡/sup¿ Ne in Cosmic Rays*, The Astrophysical Journal, 590, 822

Higdon J. C., Lingenfelter R. E., 2005, *OB Associations, Supernova-generated Superbubbles, and the Source of Cosmic Rays*, The Astrophysical Journal, 628, 738

Hillas A. M., 2006, *Cosmic Rays: Recent Progress and some Current Questions*

Hoerandel J. R., 2004, *Models of the Knee in the Energy Spectrum of Cosmic Rays*,] 10.1016/j.astropartphys.2004.01.004

Hunt E. L., Reffert S., 2023, *Improving the open cluster census. II. An all-sky cluster catalogue with Gaia DR3*,] 10.1051/0004-6361/202346285

Klepach E., Ptuskin V., Zirakashvili V., 2000, *Cosmic ray acceleration by multiple spherical shocks*, Astroparticle Physics, 13, 161

Longair M. S., 2011, *High Energy Astrophysics*. Cambridge University Press

Malcom.S.Longair 2011, *High Energy Astrophysics*. Cambridge University Press

Montmerle T., 1979, *On gamma-ray sources, supernova remnants, OB associations, and the origin of cosmic rays*, The Astrophysical Journal, 231, 95

Morlino G., Blasi P., Peretti E., Cristofari P., 2021, *Particle acceleration in winds of star clusters*, Monthly Notices of the Royal Astronomical Society, 504, 6096

Peron G., Aharonian F., Casanova S., Zanin R., Romoli C., 2020, *On the gamma-ray emission of W44 and its surroundings*,] 10.3847/2041-8213/ab93d1

Prantzos N., 2012, *On the origin and composition of Galactic cosmic rays*, Astronomy & Astrophysics, 538, A80

Sun X.-N., Yang R.-Z., Liang Y.-F., Peng F.-K., Zhang H.-M., Wang X.-Y., Aharonian F., 2020, *Diffuse ¡i¿¡/i¿ -ray emission toward the massive star-forming region, W40*, Astronomy & Astrophysics, 639, A80

T.K. Stanev T. G., 2006, *High-energy cosmic rays*

Tatischeff V., Gabici S., 2018, *Particle Acceleration by Supernova Shocks and Spallogenic Nucleosynthesis of Light Elements*, Annual Review of Nuclear and Particle Science, 68, 377

Tavani M., et al., 2010, *Direct Evidence for Hadronic Cosmic-Ray Acceleration in the Supernova Renmant IC 443*,] 10.1088/2041-8205/710/2/L151

Vallenari A., et al., 2023, *¡i¿Gaia¡/i¿ Data Release 3*, Astronomy & Astrophysics, 674, A1

Vieu T., Gabici S., Tatischeff V., Ravikularaman S., 2022, *Cosmic ray production in superbubbles*,] 10.1093/mnras/stac543

Weaver R., McCray R., Castor J., Shapiro P., Moore R., 1977, *Interstellar bubbles. II - Structure and evolution*, The Astrophysical Journal, 218, 377

Yadav N., Mukherjee D., Sharma P., Nath B. B., 2016, *How multiple supernovae overlap to form superbubbles*,] 10.1093/mnras/stw2522

collaboration T. F., Abdo A. A., 2010, *Observations of the Large Magellanic Cloud with Fermi*,] 10.1051/0004-6361/200913474

collaboration F.-L., et al., 2022, *Incremental Fermi Large Area Telescope Fourth Source Catalog*,] 10.3847/1538-4365/ac6751

zhi Yang R., Aharonian F., 2017, *Diffuse ¡i¿¡/i¿ -ray emission near the young massive cluster NGC 3603*, Astronomy & Astrophysics, 600, A107

zhi Yang R., na Sun X., Aharonian F., 2016, *On the energy distribution of relativistic electrons in the young supernova remnant G1.9+0.3*,] 10.1051/0004-6361/201630212

zhi Yang R., de Oña Wilhelmi E., Aharonian F., 2018, *Diffuse ¡i¿¡/i¿ -ray emission in the vicinity of young star cluster Westerlund 2*, Astronomy & Astrophysics, 611, A77

Appendix A

AIC test

Spatial model	$\mathcal{L}$	Δk	AIC
Single point source	8898852.145	2	-17797700.29
2 point sources	8898854.179	4	-17797700.358
Extended source	8898860.544	3	-17797719.088

Table 5.1: AIC values for 3 models of source 4FGL J1928.4+1801c, smallest AIC value is taken as the best fitting spatial model (given in green color)

Spatial model	$\mathcal{L}$	Δk	AIC
Single point source	16251542.476	2	-32503080.952
2 point sources	16251567.529	4	-32503127.058
Extended source	16251605.306	3	-32503208.612

Table 5.2: AIC values for 3 models of source 4FGL J1848.6-0202c, smallest AIC value is taken as the best fitting spatial model (given in green color)

Spatial model	$\mathcal{L}$	Δk	AIC
Single point source	16665193.864	2	-33330383.728
2 point sources	16665195.628	4	-33330383.256
Extended source	16665202.656	3	-33330403.312

Table 5.3: AIC values for 3 models of source 4FGL J1834.7-0724c, smallest AIC value is taken as the best fitting spatial model (given in green color)

Appendix B

Additional sources added in Fermi analysis

Source 4FGL J1928.4+1801c

name	point type	GLON	GLAT	spatial model	spatial width
B	circle	51.2456864	-0.447677	Radial disk	1800.000”
C	circle	50.2276821	0.2586274	Radial disk	1440.000”
D	point	53.8038219	0.3159884	point source	nan
F	point	54.7972103	-0.3165765	point source	nan
E	point	55.3727045	2.1591888	point source	nan

Table 5.4: Additional sources added to model the source, illustrated in figure 5.2

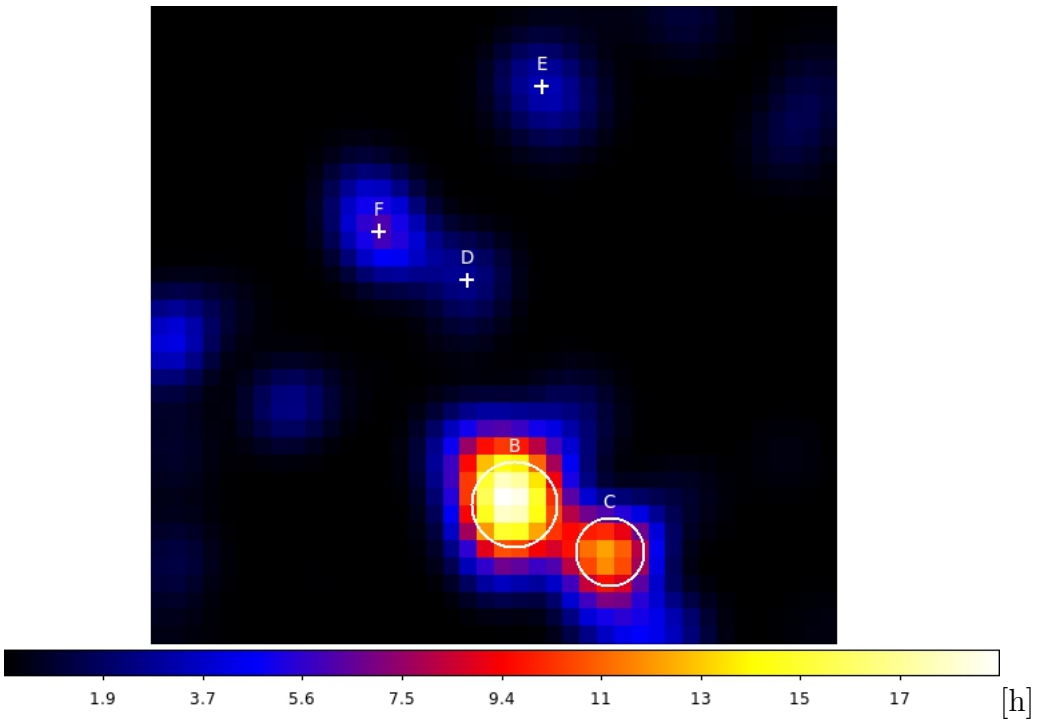

Figure 5.1: TS map marked with additional source positions added to model the source 4FGL J1928.4+1801c given in Table 5.4

Source 4FGL J1848.6-0202c

name	point type	GLON	GLAT	spatial model	spatial width
B	circle	34.1071907	0.0437589	Radial disk	1260.000”
C	circle	32.1526089	-0.6871903	Radial disk	1440.000”
F	point	32.7982213	2.363309	Point source	nan
D	point	31.2602997	0.5718102	Point source	nan
E	point	29.2902323	0.2350386	Point source	nan
H	point	29.1469086	3.2127498	Point source	nan
G	point	27.8360893	0.3664306	Point source	nan

Table 5.5: Additional sources added to model the source, illustrated in figure 5.3

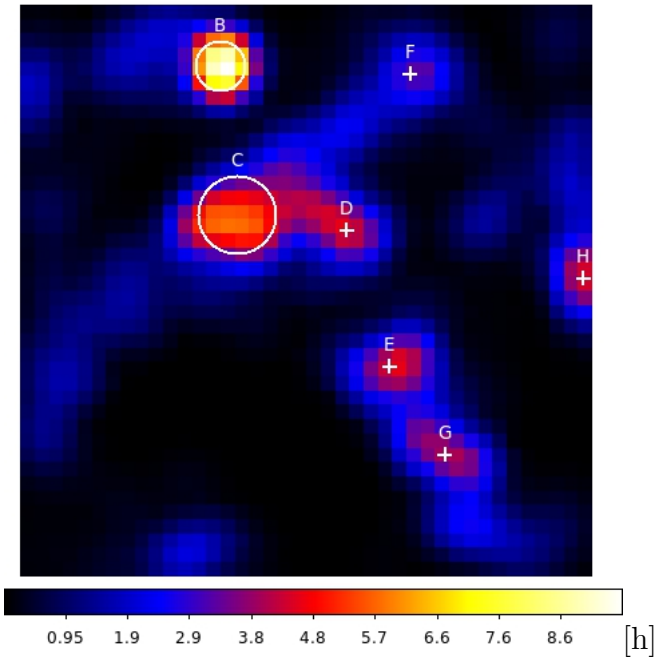

Figure 5.2: TS map marked with additional source positions added to model the source 4FGL J1848.6-0202c given in Table 5.5

Source 4FGL J1834.7-0724c

name	point type	GLON	GLAT	spatial model	spatial width
B	circle	25.9897999	0.6602178	Radial disk	1260.000”
C	circle	20.1129079	1.8043272	Radial disk	1080.000”
G	point	26.2207279	-2.7149944	Point source	nan
F	point	24.9103964	-3.349933	Point source	nan
H	point	24.8745236	-1.2779148	Point source	nan
E	point	21.3807985	0.2135823	Point source	nan
D	point	21.1549202	2.6990319	Point source	nan
J	point	28.6665764	0.2083567	Point source	nan
I	point	27.5875954	0.5681444	Point source	nan

Table 5.6: Additional sources added to model the source, illustrated in figure 5.4

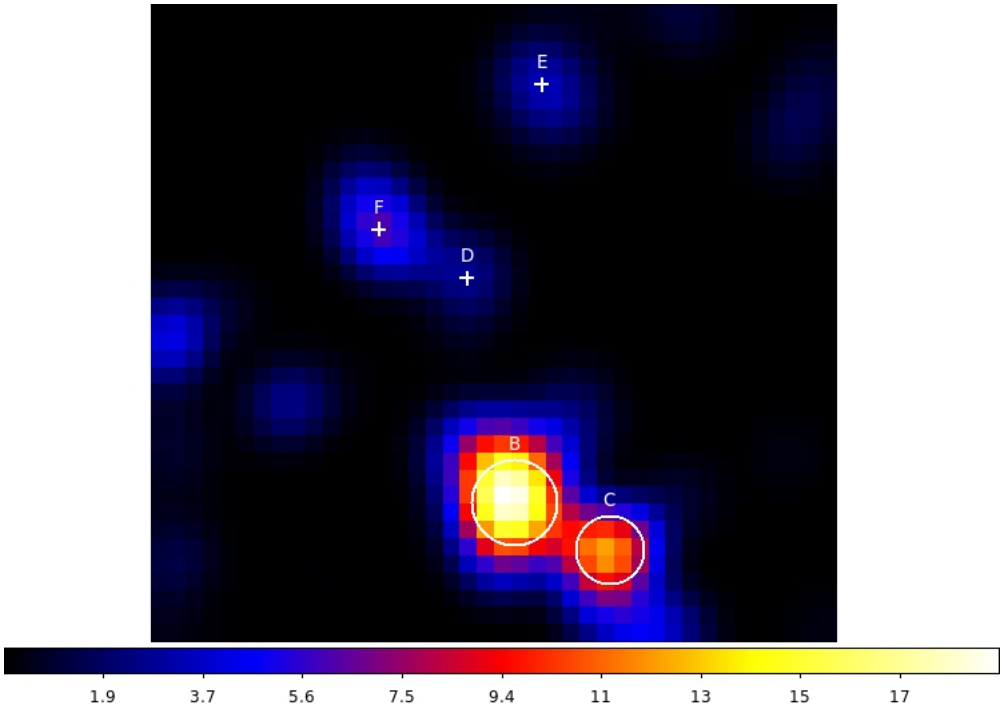

Figure 5.3: TS map marked with additional source positions added to model the source 4FGL J1834.7-0724c given in Table 5.5